

# Intense $\gamma$ -photon and high-energy electron production by neutron irradiation: effect of nuclear excitation on transport of defects

Luca Reali,<sup>\*</sup> Mark R. Gilbert,<sup>†</sup> Max Boleininger,<sup>‡</sup> and Sergei L. Dudarev<sup>§</sup>  
*CCFE, United Kingdom Atomic Energy Authority,  
 Culham Science Centre, Oxfordshire OX14 3DB, UK*

Effects of neutron irradiation on materials are often interpreted in terms of atomic recoils, initiated by neutron impacts and producing crystal lattice defects. We find that, in addition, there is a remarkable two-step process, strongly pronounced in heavy elements, involving the generation of energetic  $\gamma$ -photons in non-elastic collisions of neutrons with atomic nuclei followed by the production of high-energy electrons through the scattering of  $\gamma$ -photons by the atomic electrons. This two-step scattering creates a non-equilibrium steady-state population of high-energy electrons in the bulk of the material, which bombard atoms and stimulate vacancy diffusion, resulting in a variety of driven athermal microstructural reactions including the enhanced recombination of radiation defects. We find that tungsten converts the energy of fusion or fission neutrons into a flux of  $\gamma$ -radiation and subsequently high-energy electrons with the conversion efficiency approaching 99%, explaining the low defect content observed at moderate temperatures.

## I. INTRODUCTION

Neutron irradiation alters the microstructure of a material by producing atomic scale defects. These defects interact and coalesce, forming extended dislocation networks and voids. This ultimately results in macroscopic swelling and dimensional changes, influencing the engineering design of reactor components, similarly to the effect of thermo-mechanical and electromagnetic loads. Populations of defects act as microscopic sources for the macroscopic fields of stress and strain [1]. These populations evolve, driven by the combined effects of stochastic generation of defects by neutron and ion impacts, elastic interaction between the defects, thermal migration and athermal relaxation. The resulting pattern of microstructural evolution depends on the irradiation dose rate, temperature, and stress. The goal of nuclear fission or fusion power generation is to exploit the energy of the neutrons, produced by the decay of actinide nuclear fuel or by the deuterium-tritium fusion reactions in plasma, and it is this energy that is ultimately deposited in the coolant, structural materials or the tritium-generating fusion reactor blanket.

One way this energy deposition occurs is through elastic collisions of neutrons with the atomic nuclei. Primary knock-on atoms (PKA) initiate displacement cascades that melt the material on atomic length and time scales, leading to what is known as neutron heating. Another energy deposition mechanism involves inelastic collisions of neutrons with the nuclei, either in the form of neutron capture reactions at low neutron energies or nuclei break-up reactions at higher (MeV) energies. These and other nuclear reactions excite the internal degrees of

freedom of atomic nuclei and give rise to the generation of energetic photons through the subsequent nuclear de-excitation. This process of absorption of these energetic photons is known as  $\gamma$ -heating. It has long been realised that  $\gamma$ -heating depends strongly on the atomic weight of an element and can be the dominant heating process, more intense than heating through atomic recoils, for example by a factor of ten in niobium [2]. It is also known that  $\gamma$ -photons can produce high concentration of radiation defects in covalent and ionic crystals even if they do not displace atoms from their lattice sites [3].

Exposure to neutrons is characterised by the magnitude of the total neutron flux and its energy spectrum. The  $\gamma$ -photon flux, and in turn the high-energy electron flux that the  $\gamma$ -photons produce in a material, also have their own energy spectra. The energy spectra of all the three types of particles determine the likelihood of various scattering events via the energy dependence of the corresponding cross sections.

Electron irradiation on its own has been extensively used in the studies of production and evolution of defects in transmission electron microscopy (TEM) [4–7]. Below, we show that in the nuclear environments — whether fission or fusion — both neutron and electron irradiation are *always* present simultaneously. Notably, there are no  $\gamma$ -photons and high-energy electrons generated during ion irradiation, a fact that is not usually highlighted when comparing neutron and ion irradiation experiments [8, 9].

Interaction between high-energy electrons and atoms in a crystal can generate new defects *and* drive their subsequent motion [5, 10]. The maximum recoil energy  $E_R^{\max}$  that an atom of mass  $M$  can receive in a collision with an electron of kinetic energy  $E_{\text{el}}$  and mass  $m$  is [10, 11]

$$E_R^{\max} = \frac{2(E_{\text{el}} + 2mc^2)}{Mc^2} E_{\text{el}}, \quad (1)$$

where  $c$  is the speed of light. For instance, if  $E_{\text{el}} = 3$  MeV then in tungsten  $E_R^{\max} = 140.8$  eV, which is nearly twice the threshold displacement energy (TDE) [12, 13], the

<sup>\*</sup> Luca.Reali@ukaea.uk

<sup>†</sup> Mark.Gilbert@ukaea.uk

<sup>‡</sup> Max.Boleininger@ukaea.uk

<sup>§</sup> Sergei.Dudarev@ukaea.uk

minimum energy required to generate a stable vacancy-interstitial pair. If  $E_{e1} = 500$  keV, then  $E_R^{\text{max}} = 8.9$  eV, which is about five times the vacancy migration energy in pure elemental W [14]. Vacancy migration in W, driven by electron impacts, is observed under a 500 keV electron beam in a transmission electron microscope even at cryogenic temperatures [5]. Similarly, athermal vacancy diffusion was reported in Zr illuminated by a 800 keV electron beam at 150 K [7], and in Pb exposed to a beam of 390 keV electrons at 58 K [15]. The accelerated diffusion of vacancies stimulates rapid microstructural evolution, involving the shrinkage of interstitial-type dislocation loops [5] and growth of vacancy-type loops [7]. Electron irradiation also stimulates the motion of defect clusters at low temperatures in a variety of alloys and steels [16] and even in covalent materials like SiC [17].

Athermal vacancy migration, induced by electron impacts, was modelled using molecular dynamics (MD) by Xu *et al.* in W [12] and Satoh *et al.* in Fe and Cu [18]. They found that the minimum recoil energy for displacing a vacancy was directionally anisotropic, and strongly varied as a function of distance from a vacancy. Satoh *et al.* [18] quantified the probability of a driven vacancy hop as a function of recoil energy  $E_R$ , the distance between an atom impacted by an electron and a vacancy, and temperature. Even at high  $E_R$ , approaching 20-100 times the vacancy migration energy, the probability of an electron impact on a nearest neighbour atom resulting in a vacancy hop remains close to 0.3-0.5. This probability is higher at 300 K than at 20 K, particularly at low  $E_R$ .

Below, we detail the generation of  $\gamma$ -photons in a reactor environment and its contribution to nuclear heating in various materials. We explain how the photon spectra are derived from the neutron spectra, and how the high-energy electron spectra are related to the  $\gamma$ -photon spectra. Then, we simulate and analyse the effect of collisions between the high-energy electrons and atoms in a lattice, and quantify a relationship between atomic recoils and vacancy diffusion. Finally, we combine all the above steps and evaluate the rates of neutron- $\gamma$ -electron-stimulated vacancy migration in irradiated materials.

## II. $\gamma$ -PHOTONS PRODUCED BY EXPOSURE TO FISSION AND FUSION NEUTRONS

There are various sources of  $\gamma$ -photons (or  $\gamma$ -rays or  $\gamma$ -radiation) in a nuclear reactor environment. In addition to  $\gamma$ -photons, which are often produced by nuclei decay, it is also possible to produce X-rays or, equivalently, the Röntgen photons, which are commonly generated through the de-excitation of atomic electrons [19]. These two forms of electromagnetic radiation are fundamentally similar and there is no universally agreed differentiation between X-rays and  $\gamma$ -photons. X-rays are defined as photons with energies below 100 keV, a value that, as we shall see later, is conveniently close to the cut-off energy threshold below which the energy of the electrons

produced by the absorption of photons is too low to influence the dynamics of atoms. The  $\gamma$ -photons have the energies in the range from 100 keV to 10 MeV [20]. In this study, we investigate the  $\gamma$ -photons produced by the relaxation of atomic nuclei from their excited high energy configurations.

In fusion, the energy released in D-T reactions is carried by neutrons and  $\alpha$ -particles, formed in these events. Other types of fusion reactions are also possible, but the international fusion research is focused primarily on the D-T route.  $\gamma$ -photons with energies of 16.75 MeV and 13.5 MeV are occasionally produced in D-T reactions, and this involves the formation of a  ${}^5\text{He}$  particle instead of the dominant  $\alpha$ -particle ( ${}^4\text{He}$ ). The branching ratio for the  ${}^5\text{He}$  channel is very low compared to the main channel. Inertial confinement fusion and accelerator-based experiments show that the branching ratio for the  $\gamma$ -photon production directly from D-T reactions is in the range from  $10^{-4}$  to  $5 \times 10^{-5}$  [21]. Thus, this flux of  $\gamma$ -photons originating directly from the D-T reactions in the fusion plasma is negligible.

Meanwhile, the  $\alpha$ -particles produced in the D-T reactions do not have the sufficient energy to induce any of the nuclear reactions in the plasma-facing materials that could lead to  $\gamma$ -photon emission. The threshold minimum energies for reactions such as  $(\alpha, n)$ , in other words the  $\alpha$ -absorption followed by neutron emission, which could lead to excited isomeric states and thus  $\gamma$ -photons production analysed below, are typically above the maximum 3.5 MeV energy of  $\alpha$ -particles produced in D-T collisions, even for metals lighter than tungsten [22–24]. The direct absorption reactions  $(\alpha, \gamma)$  resulting in the photon production, are extremely rare [25]. Therefore, the only significant source of photons in a fusion reactor are the neutrons produced by the D-T reactions themselves, or those created by neutron multiplications, interacting with the nuclei in the reactor materials.

In fission, the situation is more complex. Only a relatively small proportion of the  $\sim 200$  MeV energy released in the fission of  ${}^{235}\text{U}$  is carried by neutrons – an average of around 5 MeV per fission event, whereas the vast majority ( $\sim 80\%$ ) is carried by the fission fragments themselves [20]. Additionally, prompt  $\gamma$ -photons, emitted within  $10^{-14}$  s of a fission event, typically carry around 8 MeV, while the decay of fission fragments releases around 19 MeV via  $\beta$  decays and 7 MeV through delayed  $\gamma$ -decay. The exact energy of individual  $\gamma$ -photons and  $\beta$  particles depends on the nature of the fission fragments, which vary from one fission event to another, and their decays. However, the overall intensity of  $\gamma$ -photon production is significant; for example, around 8 prompt  $\gamma$ -photons are produced per  ${}^{235}\text{U}$  fission [26], and there are of the order of  $3 \times 10^{19}$  fission events per second per GW of fission power, assuming 200 MeV of energy release per a fission event, leading to  $\sim 2.4 \times 10^{20}$   $\gamma$ -photons per GW per second.

Such a large flux of photons could be problematic to structural components, were it not for the relatively short

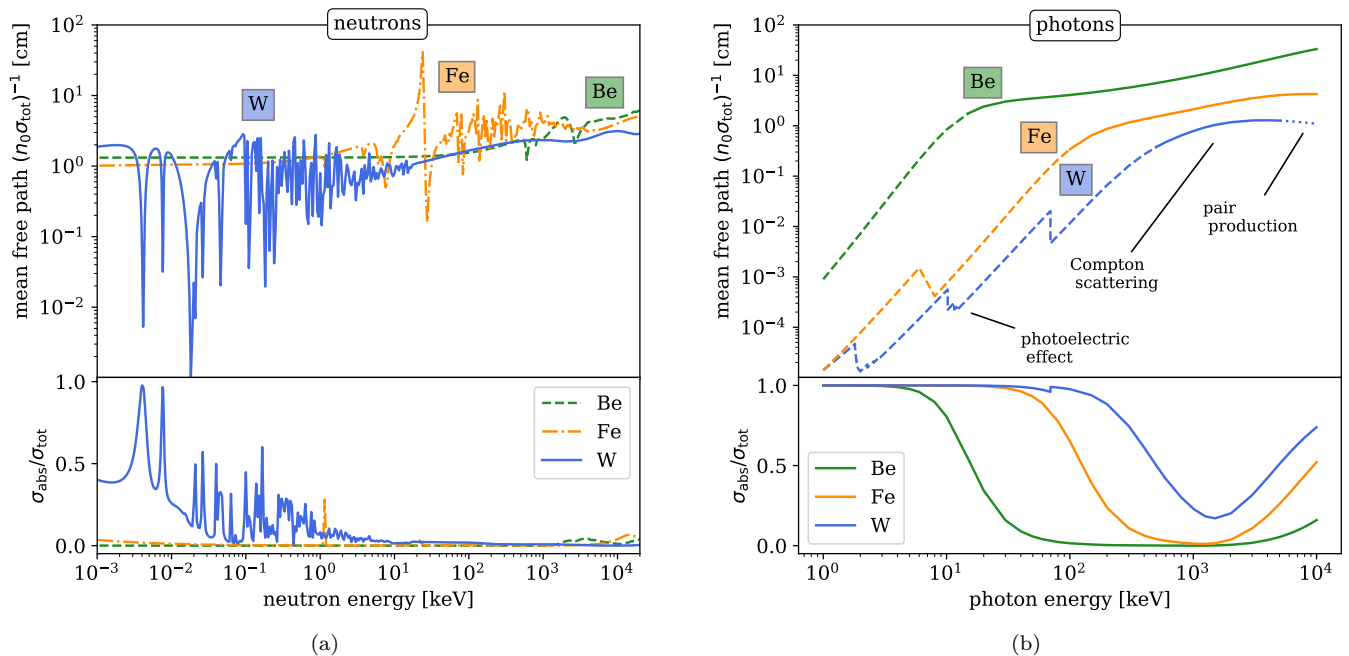


Figure 1. Mean free paths of neutrons (a) and photons (b) in Be, Fe and W as a function of energy, defined as the reciprocal of atomic density times the total cross section. The effect of atomic number on the position and character of nuclear resonances on the energy axis is clearly visible. In (b), the dominant scattering processes are highlighted. At  $\sim$  MeV energies, neutrons likely travel between 2 to 4 cm before experiencing mostly elastic scatterings;  $\gamma$ -photons in W and Fe likely travel for 1 to 2 cm, before undergoing a Compton scattering event. The lower panels show the ratio between the absorption and total cross sections, highlighting that neutrons have a much lower likelihood of being absorbed than photons, despite their mean free paths being comparable.

penetration range of  $\gamma$ -rays compared to neutrons. For example, the  $\gamma$ -photons produced by the decay of  $^{60}\text{Co}$  have energies in the range from 1.1 to 1.4 MeV. Their absorption mean free path in stainless steel is 1.6 cm and they would lose more than 90% of their intensity within 3 cm [27]. Hence, despite the large  $\gamma$ -flux in the fuel channels themselves and for experimental material samples placed in core locations, fission does not generate an appreciable external flux of  $\gamma$ -photons. This results in the same conclusion for fission as for fusion above, namely that it can be assumed, as we will in the remainder of this paper, that the dominant and the only source of photons in a bulk structural material in a nuclear reactor is that originating from within the material itself due to the nuclear reactions triggered by the incident neutrons.

Fig. 1 shows the mean free paths of neutrons and photons in Be, Fe and W. This defines the length scale between the subsequent collision events. The penetration depth of the two types of particles also depends on the probability of them being absorbed or scattered/re-emitted, see the lower panels in Fig. 1. The relative probability of absorption can be estimated from the ratio between the absorption ( $\sigma_{\text{abs}}$ ) and total ( $\sigma_{\text{tot}}$ ) cross sections. The values were taken from the TENDL-2021 [28] and the XCOM [29] libraries for neutrons and photons, respectively. For  $\sigma_{\text{abs}}$  of photons, we considered the photoelectric effect and pair production. We find that in

the  $\gtrsim$  keV energy range, the mean free paths of neutrons and photons are comparable, but the photons are far more likely to be absorbed.

Unlike photons, neutrons undergo multiple scattering and propagate through materials over much longer distances typically of the order of 10 cm and, to a first approximation, neutron flux can be considered constant in the bulk of materials on atomic length-scales; near interfaces between materials, neutron fluxes can vary more rapidly [30], but we do not consider that case here. Fig. 2 compares the neutron spectra predicted for materials in the first wall, plasma-facing environment of a fusion reactor to that expected at typical core locations in the High-Flux Reactor (HFR) fission experimental facility in Petten, Netherlands. These spectra were obtained using the MCNP transport code [31, 32] and account for the reactor geometries – in the case of HFR for a digital model of the physical reactor, and for fusion using a recent conceptual digital design of DEMO, the next-step demonstration fusion reactor, see [33, 34] for detail. The HFR spectrum was calculated specifically for a W irradiation experiment, and this took into account the local experimental environment as opposed to assuming a generic spectrum often quoted for experimental facilities. Using this refined spectrum, analysis shows that transmutation burn-up calculations with the FISPACT-II [35] inventory code accurately predict the composition evolution of W

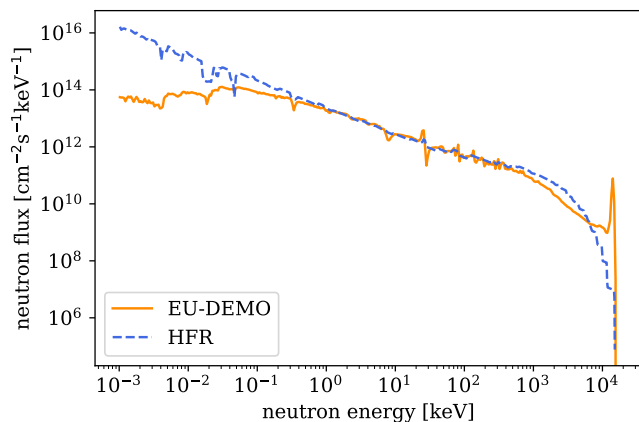


Figure 2. HFR (fission) and EU-DEMO first wall (fusion) energy-differential neutron spectra. These spectra were calculated through stochastic (Monte-Carlo) simulations by MCNP [31], and are the volume-averaged flux as a function of energy (originally in tallied histogram format, but converted to differential fluxes here by dividing by bin width). They are obtained by integrating (over angle) the energy-dependent angular flux of neutrons in a region to give the density of particles, regardless of trajectory, at a point. Over a distance element  $ds$  this density can be thought of as the track length density; MCNP estimates the average flux by summing track lengths, which is a reliable approach in well-populated statistics [31]. The resulting flux per source neutron are multiplied by the reactor power (converted to number of neutrons) to give the flux-per-second values shown.

samples placed in this environment [30, 36].

Photons are generated by various nuclear reactions involving neutrons, such as inelastic scattering, neutron multiplication ( $n,2n$ ) or neutron capture, followed by direct  $\gamma$  emission ( $n,\gamma$ ). The fundamental origin of  $\gamma$ -photon emission in all the cases is the same: when a neutron interaction leaves a daughter reaction product or nuclide in an excited state, often referred to as an isomeric state, or a metastable state if it is sufficiently long-lived, photons are emitted to release energy and allow the excited nuclei to transition through various energy levels to its lowest energy ground state. A negligibly small amount of energy is also taken by the recoiling nucleus as it decays [37]. While this ground state may also be unstable on longer time scales, producing further  $\gamma$ -photons as part of  $\beta$ -decay or  $\alpha$ -decay, these “delayed” photons are comparatively rare compared to the “prompt”  $\gamma$ -photons considered in the present work. The exact definition of prompt photons is not universally accepted, but in the context of fission reactions, prompt  $\gamma$ -photons are considered to be emitted within 10 fs of the initial reaction event [26, 38]. However, the minimum half-life for an excited nuclide to be called “isomeric”, and thus not an emitter of prompt  $\gamma$ -photons upon decay, can be anywhere from 1 ps to 1  $\mu$ s, and is often taken to be around 1 ns [20, 39]. Such metastable nuclides may persist for much longer – sometimes even for 100s or 1000s of years

– but, again, these infrequent strongly delayed  $\gamma$ -photons are not the subject of analysis here.

Instead of using a transport code to calculate the prompt photon fluxes, which is often done in complex nuclear geometries to evaluate the dose rates outside of shielding to assess the safety of maintenance operations, we can instead use an approach independent of geometry, to calculate the instantaneous source term of photons in a region exposed to a known flux and energy spectrum of neutrons. SPECTRA-PKA [40, 41] is a code developed to calculate the atomic displacement source terms due to neutron irradiation, but it can also be used to provide the equivalent  $\gamma$ -photon source terms using the available nuclear library data of  $\gamma$ -photon emission cross sections as a function of the incident neutron energy.

In what follows, we treat the photon sources and accounts for the attenuation of photons in materials while at the same time evaluating the flux of high-energy electrons generated as photons undergo interactions with *atomic* electrons. This approach, starting from a neutron spectrum for a given geometry, through a  $\gamma$ -photon source term and then  $\gamma$ -photon attenuation and electron interactions in a material, is self-consistent and avoids having to disentangle the local geometry attenuation from the pure source spectrum of  $\gamma$ -photons.

Before using SPECTRA-PKA to define the flux and energy spectrum of these local, prompt  $\gamma$ -photons, we first evaluate the neutron-induced energy deposition, often called heating. To perform these calculations, we use the FISPACT-II code, which can access the KERMA (Kinetic Energy Released per unit MAass) cross sections, expressed in barns-eV units and included in nuclear reaction data libraries. Nuclear heating is an integral measure of the energy transferred to the material by neutron irradiation. By analysing the constituent contributions to this heating, we can understand the relative significance and microscopic effects resulting from the nuclear heating caused by the  $\gamma$ -photons.

Table I summarizes FISPACT-II nuclear heating calculations for W, Fe and Be, assuming exposure to the two neutron spectra shown in Fig. 2, and hence enabling the comparison of fusion (DEMO) and fission (HFR) irradiation environments. The total nuclear heating, given in W/g units, includes the energy deposited as a result of elastic, inelastic and non-elastic (break-up) nuclear reactions initiated by neutrons, as well as any locally deposited energy from emitted secondary particles, including  $\gamma$ -photons. The table also details the absolute and relative contributions to the total heating due to the energy deposited by photons. The KERMA cross sections used here were evaluated for the TENDL-2017 [42] nuclear data library by the NJOY processing code [43, 44], assuming local absorption of the prompt photons and thus not considering their transport and attenuation.

These FISPACT-II results represent the instantaneous heating rate at time  $t = 0$ , before any transmutation has taken place. The most striking observation from these calculations is that for W and to a lesser extent for Fe,

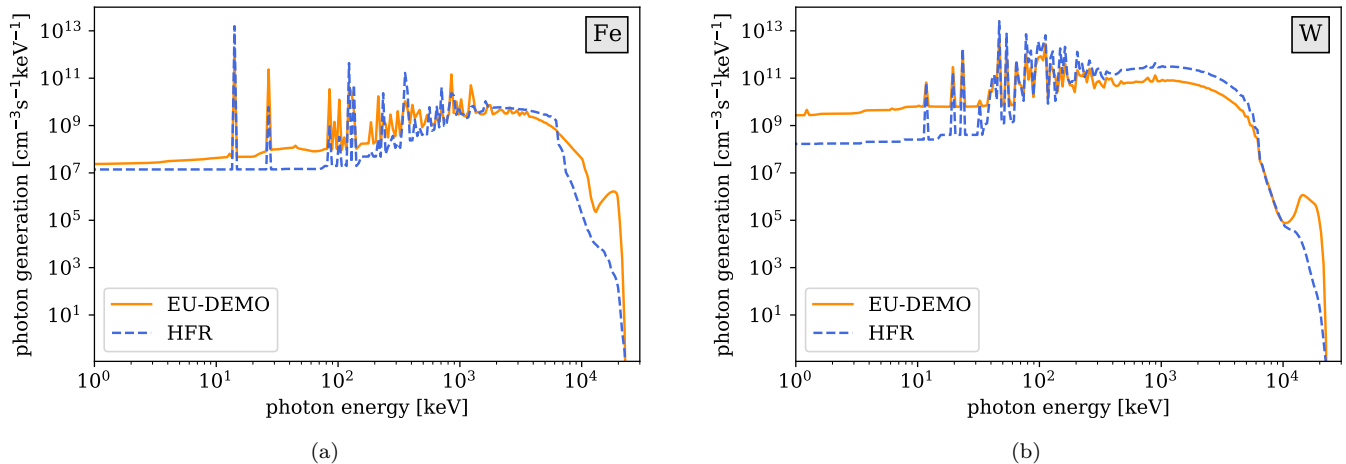


Figure 3. Source photon distributions computed using the SPECTRA-PKA code for the neutron spectra shown in Fig. 2.  $\gamma$ -photon intensities in beryllium are negligible and omitted, see Table I. The curves give the energy-resolved values of the source term  $Q_{\text{ph}}(E)$ , defined by Eq. (10) and referring to the generation of  $\gamma$ -photons per unit volume.

the two technologically most significant fusion materials [45–47],  $\gamma$ -photon heating entirely dominates the energy deposited in the material exposed to neutron irradiation under both fission and fusion conditions.

This result can be understood by considering that in high atomic mass elements like W there is a greater scope for nuclei excited states because there are more possible configurations of the nucleus in which to store energy. When the nucleon number, i.e. the total number of protons and neutrons, is high there is a significant and often dominant probability that the nuclear reaction energy will be trapped in an excited isomeric state and subsequently converted into  $\gamma$ -photons during isomeric transitions. In contrast, in simpler low nucleon number materials like Be, there are fewer isomeric possibilities and so the energy is more readily released directly in the form of kinetic energy of the daughter products of nuclear reactions.

The results summarised in Table I demonstrate how important it is to consider the effect of  $\gamma$ -photons on microstructural evolution, particularly in the critical fusion and fission nuclear materials such as W and Fe [45–47], where the energy released during nuclear reactions is dominated by the photons and not by atomic recoils. Table I shows that tungsten acts as a highly efficient converter of the energy of fusion or fission neutrons into electromagnetic  $\gamma$ -radiation, with the conversion efficiency approaching 99%.

Using the neutron spectra shown in Fig. 2 as input for SPECTRA-PKA calculations, we find the  $\gamma$ -photon flux distributions for Fe and W shown in Fig. 3. Beryllium is omitted from this figure as it generates a negligible flux of  $\gamma$ -photons, in agreement with the data given in Table I. These distributions will be used later in the paper to evaluate the flux of high-energy electrons produced by the  $\gamma$ -photons in the material, and at this point it is

Table I. Nuclear heating, detailing the contribution of  $\gamma$ -photon emission to the energy deposited in materials exposed to fusion and fission neutrons.

Material	Heating (W/g)					
	DEMO			HFR		
	Total	Photon	Fraction	Total	Photon	Fraction
W	2.73	2.65	97.0%	10.48	10.36	98.9%
Fe	1.68	1.19	70.8%	2.00	1.63	81.5%
Be	3.65	$3 \times 10^{-3}$	0.1%	2.15	$8 \times 10^{-7}$	$4 \times 10^{-5}\%$

instructive to highlight the fundamental origin of spectra of  $\gamma$ -photons. To illustrate the principle, in Fig. 4 we plot the dominant channel contributions for W under fusion (DEMO) and fission (HFR) conditions. In both cases we see an overwhelming dominance of the neutron capture ( $n, \gamma$ ) reactions, particularly at higher  $> \text{MeV}$   $\gamma$ -photon energies.

In what follows, we assume that the  $\gamma$ -photons emitted by the excited nuclei, and the high-energy electrons that these  $\gamma$ -photons produce in a material, are generated isotropically and their flux has no directional dependence. The neutron flux in a nuclear reactor inevitably has some angular anisotropy because, for example, the 14.1 MeV neutrons produced in a fusion plasma initially travel radially away from the plasma, whereas the lower energy neutrons originating from multiple scattering events in the surrounding structure have a strong back-scattered component. Any directional dependence of the neutron flux is lost at low energies due to multiple scattering. Similarly, in fission, there is a directional dependence of the fast (above 1 MeV) neutron flux emitted from the fuel pins, which impinges on the surrounding structural materials, but the high thermal component shown in Fig. 2 is directionally more isotropic.

The prompt  $\gamma$ -photons are generated in materials pri-

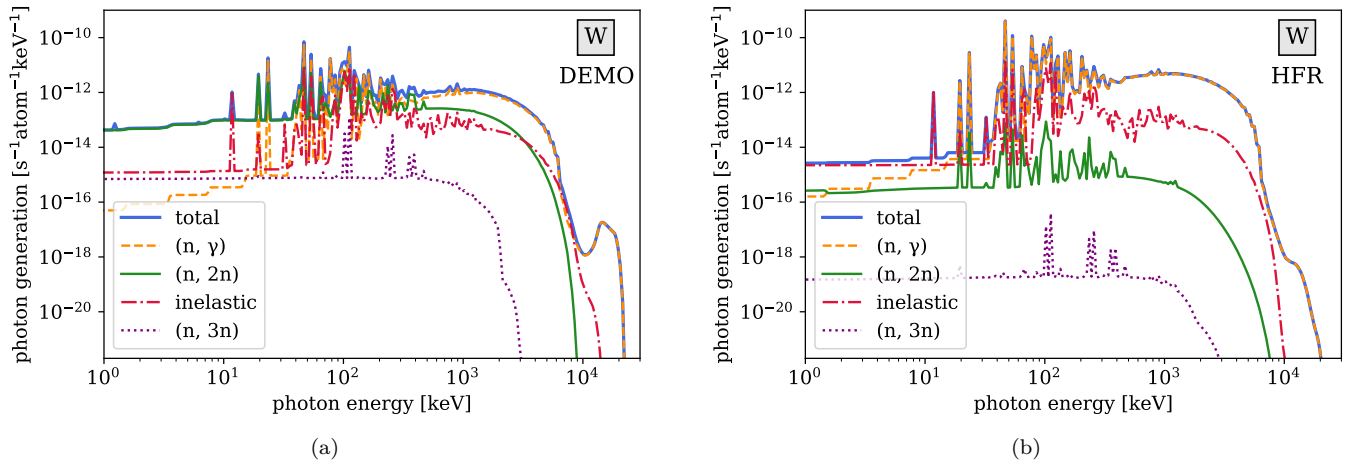


Figure 4. Various nuclear reaction channel contributions to the  $\gamma$ -photon generation in W. Left panel: spectrum of photons generated by fusion neutrons, right panel: spectrum of photons produced by fission neutrons. Fusion and fission neutron spectra are taken from Fig. 2. The curves give the energy-resolved values of the source term  $Q_{\text{ph}}(E)$ , defined by Eq. (10) and referring to the generation of  $\gamma$ -photons by an individual atomic nucleus.

marily from the neutron capture  $(n, \gamma)$  or inelastic scattering reactions, and can have angular anisotropy associated with the initial direction of the neutron momentum transferred to the compound nucleus [48], as observed in inelastic scattering experiments on iron [49].  $\gamma$ -radiation intensities have been found to be correlated with the direction of motion of fission fragments [50]. However, since neutron capture and inelastic scattering dominate the generation of  $\gamma$ -photons in structural materials, as illustrated in Fig. 4, and since these reactions typically occur at MeV energies and below, especially in the case of neutron capture, most of the directional dependence on the neutron flux will have been lost at the point of  $\gamma$ -photon production due to the multiple scattering of neutrons. It is therefore reasonable to assume the angular isotropy of the flux of  $\gamma$ -photons. The flux of electrons  $\phi_{\text{el}}(\mathbf{n}, E)$ , produced by the scattering of  $\gamma$ -quanta, is also isotropic, and in the absence of directional variables is solely a function of the kinetic energy of the electrons.

### III. ENERGY SPECTRA OF $\gamma$ -PHOTONS AND HIGH-ENERGY ELECTRONS

A quantity central to the treatment of rates of scattering, atomic recoils, and reactions in solids, is the flux of high-energy particles initiating the respective scattering and reaction events. This flux, denoted by  $\phi(\mathbf{n}, \mathbf{r}, E)$ , equals the number of particles or photons with kinetic energy  $E$  that cross a unit area in the direction of unit vector  $\mathbf{n}$  per unit time in the vicinity of point  $\mathbf{r}$ . This flux can be computed by multiplying the density  $f(\mathbf{n}, \mathbf{r}, E)$  of particles with kinetic energy  $E$ , and moving in direction  $\mathbf{n}$ , by their velocity  $v$ .

For example, if  $\phi_{\text{el}}(\mathbf{n}, \mathbf{r}, E)$  is the flux of high energy electrons, the rate of scattering of electrons by an atom

located at  $\mathbf{r}$  is

$$\frac{d^2\sigma(\mathbf{n}, E \rightarrow \mathbf{n}', E')}{d\mathbf{o}'dE'}\phi_{\text{el}}(\mathbf{n}, \mathbf{r}, E), \quad (2)$$

where  $d^2\sigma/d\mathbf{o}'dE'$  is the differential cross section of scattering of electrons into an element of solid angle  $d\mathbf{o}'$  corresponding to direction  $\mathbf{n}'$ , and an energy interval  $dE'$ . If the flux of electrons is mono-energetic then integrating (2) over all the directions of scattering  $\mathbf{n}'$  and energies  $E'$ , as well over the directions of incidence  $\mathbf{n}$ , we find the total rate of collisions of electrons with an atom situated at  $\mathbf{r}$ , namely

$$\nu_{\text{tot}}(E, \mathbf{r}) = \sigma_{\text{tot}}(E) \int d\mathbf{o} \phi_{\text{el}}(\mathbf{n}, \mathbf{r}, E). \quad (3)$$

The total cross section of scattering

$$\sigma_{\text{tot}}(E) = \int d\mathbf{o}' \int dE' \frac{d^2\sigma(\mathbf{n}, E \rightarrow \mathbf{n}', E')}{d\mathbf{o}'dE'} \quad (4)$$

is independent of  $\mathbf{n}$  due to the rotational invariance of the process of scattering, requiring that the differential cross section depends only on the angle between vectors  $\mathbf{n}$  and  $\mathbf{n}'$  [51, 52].

In the treatment of threshold atomic recoil events below, we explore quantities similar to (3), and often involving integration over a selected range of solid angles corresponding to a reaction, for example a hop of an atom from an occupied to a vacant lattice site. Such a hop occurs only if the direction of the recoil is favourable and is able to initiate a transition along a trajectory that crosses the energy barrier for the reaction.

The flux of neutrons, electrons or photons satisfies the Boltzmann transport equation [53, 54], extensively used in the theory of radiative transfer [55], namely

$$\mathbf{n} \cdot \frac{\partial}{\partial \mathbf{r}} \phi(\mathbf{n}, \mathbf{r}, E) = I_{\text{coll}}[\phi(\mathbf{n}, \mathbf{r}, E)] + Q(\mathbf{n}, \mathbf{r}, E). \quad (5)$$

In this equation,  $I_{\text{coll}}[\phi(\mathbf{n}, \mathbf{r}, E)]$  is the so-called collision term that describes the effect of scattering by atoms or nuclei on the propagation of particles through the material, and  $Q(\mathbf{n}, \mathbf{r}, E)$  is the source term accounting for the generation of particles. For example, in the Boltzmann transport equation for high-energy electrons,  $Q(\mathbf{n}, \mathbf{r}, E)$  describes the generation of electrons by the  $\gamma$ -photons, whereas in the transport equation for  $\gamma$ -photons the source term refers to the generation of photons by the relaxation of excited states of atomic nuclei [56].

For the  $\gamma$ -photons generated by neutrons, the source term has the form

$$\begin{aligned} & Q_{\text{ph}}(\mathbf{n}_\gamma, \mathbf{r}, E_\gamma) \\ &= n_0 \int d\sigma' d\sigma \int dE' dE \frac{d^2 \sigma_{n\gamma}(\mathbf{n}', E' \rightarrow \mathbf{n}, E; \mathbf{n}_\gamma, E_\gamma)}{d\sigma' dE'} \\ & \quad \times \phi_n(\mathbf{n}', \mathbf{r}, E'), \end{aligned} \quad (6)$$

where  $n_0$  is the number density of atomic nuclei,  $\phi_n(\mathbf{n}', \mathbf{r}, E')$  is the flux of neutrons interacting with the nuclei, and

$$\frac{d^2 \sigma_{n\gamma}(\mathbf{n}', E' \rightarrow \mathbf{n}, E; \mathbf{n}_\gamma, E_\gamma)}{d\sigma' dE'} \quad (7)$$

is the differential cross section of scattering of a neutron by an atomic nucleus, with the neutron changing its direction of propagation and energy from  $(\mathbf{n}', E')$  to  $(\mathbf{n}, E)$ , accompanied by the production of a  $\gamma$ -photon with energy  $E_\gamma$  travelling in the direction  $\mathbf{n}_\gamma$ . The integration of (6) over directions  $\mathbf{n}_\gamma$  and energies  $E_\gamma$  gives the total number of  $\gamma$ -photons generated in a unit volume of the material per unit time. This quantity can also be computed numerically. For example, the curves shown in Figs. 3 and 4 were computed using Monte Carlo MCNP simulations. They are equivalent to integrating Eq. (6) over directions  $\mathbf{n}_\gamma$  but not energies  $E_\gamma$ , yielding the source term in a form differential with respect to the energy of photons  $E_\gamma$ .

Eq. (5) itself in some cases can be solved analytically [53, 55], but more often its solutions are found numerically using Monte Carlo methods [54, 57], see Ref. [58] for more detail.

The collision term in the right-hand side of the Boltzmann transport equation (5) has the form [53, 54]

$$\begin{aligned} & I_{\text{coll}}[\phi(\mathbf{n}, \mathbf{r}, E)] = -n_0 \sigma_{\text{tot}}(E) \phi(\mathbf{n}, \mathbf{r}, E) \\ & + n_0 \int d\sigma' \int dE' \frac{d^2 \sigma(\mathbf{n}', E' \rightarrow \mathbf{n}, E)}{d\sigma' dE'} \phi(\mathbf{n}', \mathbf{r}, E'), \end{aligned} \quad (8)$$

where  $n_0$  is the number density of atoms or, equivalently, atomic nuclei in the material, and integration over  $d\sigma'$  and  $dE'$  is performed over the solid angle and energy of particles scattered by these atoms or nuclei. The first, negative, part of the collision term in (8) describes the differential rate of loss of flux from an element of phase space  $(\mathbf{n}, E)$ , whereas the second part of the collision term accounts for the rate of scattering *into* this element

of phase space. If absorption is the dominant channel of scattering, only the first, negative, term needs to be retained in the right-hand side of (8).

When the above equations are applied to the treatment of transport of high-energy electrons, velocity  $\mathbf{v} = v\mathbf{n}$  of an electron is related to its momentum  $\mathbf{p}$  through the relativistic kinematic formula  $\mathbf{p} = m\mathbf{v}/\sqrt{1 - v^2/c^2}$ . The kinetic energy of an electron is  $E = c\sqrt{p^2 + m^2 c^2} - mc^2$  [59], where  $p = |\mathbf{p}|$  and  $c$  is the speed of light.

### A. Photons: iterative solution of the transport equation

If the source of  $\gamma$ -photons is directionally isotropic and the rate of spatial variation of the field of photons is negligible in comparison with all the other length scales involved, we can neglect the derivative with respect to spatial coordinates in the left-hand side of (5), and arrive at

$$I_{\text{coll}}[\phi_{\text{ph}}(E)] + Q_{\text{ph}}(E) = 0. \quad (9)$$

The angularly isotropic photon flux and the source term, shown in Figs. 3 and 4, are

$$\begin{aligned} \phi_{\text{ph}}(\mathbf{n}, E) &= \frac{1}{4\pi} \phi_{\text{ph}}(E), \\ Q_{\text{ph}}(\mathbf{n}, E) &= \frac{1}{4\pi} Q_{\text{ph}}(E). \end{aligned} \quad (10)$$

In this approximation, the collision term (8) transforms to

$$\begin{aligned} & I_{\text{coll}}[\phi_{\text{ph}}(E)] = -n_0 \sigma_{\text{tot}}(E) \phi_{\text{ph}}(E) \\ & + n_0 \int dE' \phi_{\text{ph}}(E') \int d\sigma' \frac{d^2 \sigma(\mathbf{n}', E' \rightarrow \mathbf{n}, E)}{d\sigma' dE'}. \end{aligned} \quad (11)$$

By denoting the kernel of the integral over the solid angle  $d\sigma'$  in (11) by

$$K(E, E') = \int d\sigma' \frac{d^2 \sigma(\mathbf{n}', E' \rightarrow \mathbf{n}, E)}{d\sigma' dE'}, \quad (12)$$

we arrive at a closed equation for the energy spectrum of  $\gamma$ -photons

$$\begin{aligned} & Q_{\text{ph}}(E) - n_0 \sigma_{\text{tot}}(E) \phi_{\text{ph}}(E) \\ & + n_0 \int dE' K(E, E') \phi_{\text{ph}}(E') = 0. \end{aligned} \quad (13)$$

This equation can be readily solved by iteration. This involves representing the energy spectrum in the form of a series, where each term refers to the number of scattering events undergone by an energetic  $\gamma$ -photon in a material

$$\phi_{\text{ph}}(E) = \phi_{\text{ph}}^{(0)}(E) + \phi_{\text{ph}}^{(1)}(E) + \phi_{\text{ph}}^{(2)}(E) + \dots \quad (14)$$

The zero-order term in the series describes the flux of photons directly emitted by the atomic nuclei

$$\phi_{\text{ph}}^{(0)}(E) = \frac{Q_{\text{ph}}(E)}{n_0 \sigma_{\text{tot}}(E)}, \quad (15)$$

and the subsequent terms

$$\phi_{\text{ph}}^{(i)}(E) = \frac{1}{\sigma_{\text{tot}}(E)} \int dE' K(E, E') \phi^{(i-1)}(E') \quad (16)$$

refer to the contributions to the energy spectrum of  $\gamma$ -photons from trajectories involving  $i$  events of Compton scattering of photons by conduction and inner-shell atomic electrons. Expression for the kernel  $K(E, E')$  computed using (12) has the form

$$K(E, E') = \begin{cases} \frac{\pi r_c^2 mc^2}{E'^2} \left[ \frac{E}{E'} + \frac{E'}{E} - 1 + \left( \frac{mc^2}{E'} - \frac{mc^2}{E} + 1 \right)^2 \right], & \frac{E'}{1 + \frac{2E'}{mc^2}} < E < E' \\ 0, & \text{otherwise} \end{cases} \quad (17)$$

where  $r_c = 2.8179$  fm is the classical electron radius. The above formula results from inserting into Eq. (12) the Klein-Nishina cross section

$$\frac{d\sigma}{d\omega} = \frac{r_c^2}{2} \left( \frac{E'}{E} \right)^2 \left[ \frac{E'}{E} + \frac{E}{E'} - \sin^2 \theta \right], \quad (18)$$

where  $\theta$  is the photon scattering angle.

The photon generation term  $Q_{\text{ph}}(E)$  in Eqs. (6) and (15), expressed either in volumetric units  $\text{cm}^{-3}\text{s}^{-1}\text{eV}^{-1}$  in Fig. 3, or in atomic units  $\text{s}^{-1}\text{atom}^{-1}\text{eV}^{-1}$  in Fig. 4, is obtained by folding the  $(n, \gamma)$  cross section matrices with the energy-spectrum-resolved neutron flux. It is calculated internally in transport codes such as MCNP, and can also be explicitly obtained by inputting the cross sections generated by NJOY [44] into the processing code SPECTRA-PKA [40]. The cross section in the denominator of Eq. (15) and Eq. (16) depends on the photon energy. For photons in the energy range from about 10 keV to 10 MeV,  $\sigma_{\text{tot}}(E)$  is dominated by photoelectric absorption (PE, the lower end of the energy spectrum), the Compton scattering (CS, the middle part of the spectrum), or by the electron-positron pair production (PP, the upper end of the spectrum). The total cross section can be written as a sum

$$\sigma_{\text{tot}}(E) = \sigma_{\text{PE}}(E) + \sigma_{\text{CS}}(E) + \sigma_{\text{PP}}(E), \quad (19)$$

where the numerical values for individual terms are available from tables [60] or databases [29]. Of the three processes included in (19), only the Compton scattering does not lead to the absorption of photons, and hence is the only process that contributes to the scattering kernel (12).

Eq. (12) assumes that electrons in a material act as independent centres of scattering of photons, regardless of them being free or bound in the inner electronic shells of atoms. This approximation is justified if we are interested in the photon energies higher than approximately 100 keV, see Appendix A. Fig. 1 shows plots of the mean distance between photon scattering events  $[n_0 \sigma_{\text{tot}}(E)]^{-1}$

that, in the limit where absorption is dominant, determine the characteristic attenuation distance of a photon flux emitted by a localised source.

The inverse total scattering cross section is the most important scaling factor in the representation of the photon flux as a series in the number of scattering events (15) and (16). In the interval of energies where the Compton scattering dominates, photons may lose nearly half of their energy in a single scattering event, depending on the angle between directions  $\mathbf{n}$  and  $\mathbf{n}'$ . We also note that the above calculations assume that the  $\gamma$ -photons are generated in the bulk of the material and that the local flux of photons is proportional to the local flux of neutrons. If in addition there is flux of photons from an external source, it will provide an extra contribution to the various scattering events, including the generation of high-energy electrons considered in the next section.

## B. High-energy electrons: the continuous slowing down approximation

The PE, CS and PP processes, giving rise to the absorption or scattering of  $\gamma$ -photons, result in the generation of high energy electrons. Similarly to how nonelastic nuclear reactions give rise to the generation of  $\gamma$ -photons described by the source term  $Q_{\text{ph}}(E)$  in (6), the PE, CS and PP processes are responsible for the *electron* generation term  $Q_{\text{el}}(E)$  in Eq. (5). This phenomenon of production of high-energy electrons by  $\gamma$ -photons is well recognised, for example the authors of Ref. [61] note the equivalence of  $\gamma$ -photon and electron irradiation. The source term describing scattering of  $\gamma$ -photons by atoms serves as a starting point in a calculation of the flux of high-energy electrons.

If the flux of electrons is directionally isotropic and its variation on the spatial scale of the problem is negligible, we write

$$\phi_{\text{el}}(\mathbf{n}, E) = \frac{1}{4\pi} \phi_{\text{el}}(E). \quad (20)$$

The only variable characterising the flux of electrons is their energy  $E$ , and now the collision term (8) describes electron energy losses, which can be treated in the continuous slowing down approximation [53, 54, 62]. In this approximation, assuming that the flux of electrons is independent of spatial coordinates, the Boltzmann transport equation acquires the form

$$0 = \frac{\partial}{\partial E} [\bar{\varepsilon}(E) \phi_{\text{el}}(E)] + Q_{\text{el}}(E), \quad (21)$$

where  $\bar{\varepsilon}(E)$  is the average rate of energy losses of an electron with energy  $E$ , and  $Q_{\text{el}}(E)$  is the rate of generation of electrons with energy  $E$  by the  $\gamma$ -photons. The average rate of energy losses per unit distance travelled  $\bar{\varepsilon}(E)$  is related to the range  $R(E)$  of electrons in the material

via [53, 54, 63–65]

$$R(E) = \int_0^E \frac{dE'}{\bar{\varepsilon}(E')}. \quad (22)$$

Equation (21) can be readily solved, and its solution has the form

$$\phi_{\text{el}}(E) = \frac{1}{\bar{\varepsilon}(E)} \int_E^\infty Q_{\text{el}}(E') dE'. \quad (23)$$

This analytical expression describes a directionally isotropic distribution of high energy electrons (20) that energetic  $\gamma$ -photons generate in the bulk of the material. In practice the upper limit of integration in (23) is determined by the energy span of the source function  $Q_{\text{el}}(E)$ , whereas numerical values of function  $\bar{\varepsilon}(E)$  are available in literature [66]. The flux of electrons  $\phi_{\text{el}}(E)$  can also be computed numerically using Monte Carlo simulations [54, 57], and below we show that results of such simulations compare favourably with the analytical result (23).

The electron generation term has the form

$$Q_{\text{el}}(E) = Q_{\text{PE}}(E) + Q_{\text{CS}}(E) + Q_{\text{PP}}(E). \quad (24)$$

At high energies well above the keV range, we neglect the electron binding energy effects and write

$$Q_{\text{PE}}(E) = n_0 \sigma_{\text{PE}}(E) \phi_{\text{ph}}(E). \quad (25)$$

The Compton scattering contribution can be evaluated by noting that the energy balance dictates that the electron energy equals the difference between the photon energy before and after the event,  $E = E_{\text{ph}} - E'_{\text{ph}}$ . Therefore it follows from Eq. (17) that the energy-differential Compton cross section involving an electron receiving recoil energy  $E$  is

$$\frac{d\sigma}{dE} = \begin{cases} \frac{\pi r_e^2 m c^2}{E_{\text{ph}}^2} \left[ \frac{E_{\text{ph}}}{E_{\text{ph}} - E} - \frac{E}{E_{\text{ph}}} \right. \\ \left. + \left( \frac{m c^2}{E_{\text{ph}}} - \frac{m c^2}{E_{\text{ph}} - E} + 1 \right)^2 \right], & 0 < E < \frac{2E_{\text{ph}}^2}{2E_{\text{ph}} + m c^2} \\ 0, & \text{otherwise} \end{cases} \quad (26)$$

If the number density of electrons is  $n_{\text{el}}$ , the resulting electron generation term is

$$Q_{\text{CS}}(E) = n_{\text{el}} \int \phi_{\text{ph}}(E_{\text{ph}}) \frac{d\sigma}{dE}(E_{\text{ph}}, E) dE_{\text{ph}}. \quad (27)$$

If the photon flux is represented by a discrete  $N$ -point set on a grid of photon energies  $E_i$ , we can write the energy-differential flux of electrons in the form of a discrete sum of Dirac delta functions

$$\phi_{\text{ph}}(E_{\text{ph}}) = \sum_{i=1}^N \Phi_{\text{ph}}^{(i)} \delta(E_{\text{ph}} - E_i). \quad (28)$$

This then simplifies Eq. (27) to

$$Q_{\text{CS}}(E) = n_{\text{el}} \sum_{i=1}^N \Phi_{\text{ph}}^{(i)} \frac{d\sigma}{dE}(E_i, E). \quad (29)$$

Finally, high-energy electrons can be generated through the production of electron-positron pairs, resulting from the conversion of photons with energy greater than  $2mc^2 \sim 1.022$  MeV into electrons and positrons. The sum of kinetic energies of an electron and a positron is then  $E_{\text{ph}} - 2mc^2$ . Assuming that this energy is split equally between the two particles, we find that  $E = \frac{1}{2}(E_{\text{ph}} - 2mc^2)$  and

$$Q_{\text{PP}}(E) = n_0 \sigma_{\text{PP}}(E_{\text{ph}}) \phi_{\text{ph}}(E_{\text{ph}}). \quad (30)$$

Monte Carlo MCNP simulations were used for validating the approximations involved in Eq. (15) and Eq. (16) for  $\gamma$ -photons and Eq. (23) for high-energy electrons. The curves computed independently using the above equations and MCNP simulations are shown in Fig. 5. The DEMO spectrum of neutrons from Fig. 2 was used as a spatially homogeneous incident flux of neutrons in a  $20 \times 20 \times 20$  cm<sup>3</sup> cube of tungsten, with periodic boundary conditions (PBCs) applied along  $x$  and  $y$ , and reflecting planes bounding the cell in  $z$ . Neutrons, photons and electrons were tallied in the box to produce the MCNP results shown in Fig. 5. Using tallies on a grid of 8000 1 cm<sup>3</sup> voxels, we confirmed that there was no detectable spatial variation of the spectra and thus the results are representative of an effectively infinite bulk sample of W. The total neutron flux of the input source spectrum was  $5.04 \times 10^{14}$  cm<sup>-2</sup>s<sup>-1</sup>. The neutron flux calculated by MCNP was normalised to the same value. This resulting tallied neutron spectrum is slightly different from the input spectrum, shown in the top panel of the figure because, as opposed to the current simulation, the input neutron spectrum was produced in simulation assuming a thin W layer in the first wall of a full-reactor DEMO involving also other materials. Because of the high computational cost of simulating the photon and particularly electron transport in MCNP, it was not feasible to perform the N-P-E transport simulation using the full DEMO geometry. The MCNP-generated neutron flux was used for evaluating  $\phi_{\text{ph}}(E)$  through Eqs. (14), (15) and (16), and then for comparing the outcome to the MCNP  $\gamma$ -photons result. Similarly, the MCNP-generated photon flux represented input for high-energy electron flux calculations, which was then compared to the MCNP result. It is worth noting that the MCNP calculation with full photon and electron transport for this relatively simple system (single cube with no complex surfaces or long transport paths) and a relatively modest  $10^8$  source neutrons took approximately 2 days using 8 processors, whereas the calculation required of the order of seconds on a laptop.

Neutron flux used for evaluating the generation rate of  $\gamma$ -photons and high-energy electrons in Fig. 5 refers to what were to be expected if scattering occurred in pure

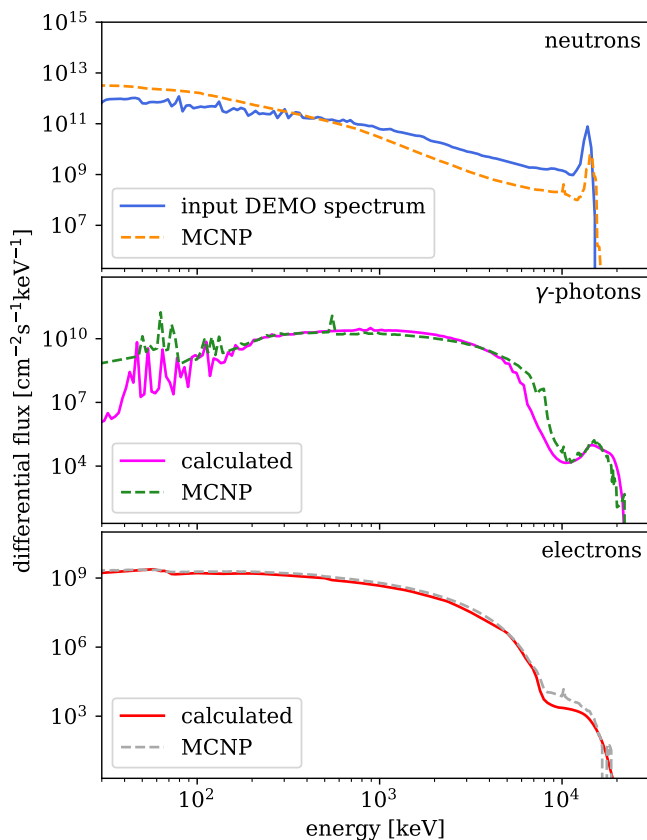


Figure 5. Top: input DEMO spectrum shown together with the neutron spectrum it generates in MCNP under periodic boundary conditions. Central and bottom panels: MCNP photon and electron spectra compared to the  $\phi_{\text{ph}}(E)$  and  $\phi_{\text{el}}(E)$  spectra computed using equations given in the text. The abscissa is the same for the three panels. Note that the two neutron spectra are different as one is representative of a thin first-wall W layer in a mixed-material DEMO reactor and the other is the result of that same spectrum being propagated through pure bulk W. The photon and electron spectra are consistent with the MCNP bulk W simulation and thus the equivalence between the MCNP and calculated curves validates the methodology for the latter.

W. In Fig. 6 and Table II we plot the curves and provide numerical data for the photon and electron spectra developing in bulk Fe and W exposed to the neutron spectra shown in Fig. 2, calculated as explained in Sec. III. In both fission and fusion scenarios the photon and electron spectra are qualitatively similar. The intensity of photon fluxes is comparable to the neutron fluxes. Notably, the neutrons generate  $\gamma$ -photon spectra with the characteristic energy of  $\sim 1 - 1.5$  MeV, and electrons spectra with the characteristic energy of  $\sim 0.5 - 1$  MeV, which are skewed towards high energies.

The characteristic scale of electron energies that we see in Fig. 6 is the same as the energy range of electrons used in transmission electron microscope experiments [5] where it was found that the flux of electrons was able to

drive microstructural evolution of the material exposed to an electron beam. In W, the photon and electron fluxes computed for the HFR input spectrum are about 4 times higher than those computed for the DEMO neutron spectrum.

#### IV. ATOMIC RECOILS PRODUCED BY HIGH-ENERGY ELECTRONS

In the treatment of scattering of energetic particles by atoms in a material, involving either the Boltzmann transport equation [53, 54] or Monte Carlo simulations [57], the fact that scattering involves not only the change of momenta of the incident particles but also atomic recoils, is often not recognised. Experimental observations and theoretical analysis [5, 67–69] show that even the relatively low energy electrons produce atomic recoils with energies in the electron-volt range, comparable with the energy barrier for vacancy migration in metals [70].

High-energy atomic recoils can be formally treated as multi-phonon excitation events, whereas at low energies it is often sufficient to retain only the lowest order single-phonon terms when computing the scattering structure factor [71]. Irrespectively of the recoil energy, electron-atom recoils can be treated as electron-phonon interaction events, resulting in the eventual dissipation of the energy of high-energy electrons into the heat bath of thermal atomic vibrations.

The treatment of relativistic collision kinematics involving an electron with mass  $m$  and an atom with mass  $M$  gives a relation between the kinetic energy of the recoil atom  $E_R$  and the angle of scattering  $\theta$ , defined in the centre of mass frame [59]

$$E_R = \frac{Mc^2 E_{\text{el}} (E_{\text{el}} + 2mc^2)}{(m + M)^2 c^4 + 2Mc^2 E_{\text{el}}} (1 - \cos \theta), \quad (31)$$

where  $E_{\text{el}}$  is the kinetic energy of the fast electron,  $E_{\text{el}} = mc^2 / \sqrt{1 - v^2/c^2} - mc^2$ , and  $\cos \theta = (\mathbf{n} \cdot \mathbf{n}')$ . In the limit  $m \ll M$ , Eq. (31) can be simplified as [6, 56, 72]

$$E_R = \frac{E_{\text{el}} (E_{\text{el}} + 2mc^2)}{Mc^2} (1 - \cos \theta). \quad (32)$$

The maximum amount of energy is transferred to an atom in a collision where the electron is scattered exactly backwards  $\theta = \pi$ . Taking  $\cos \theta = -1$ , from Eq. (32) we find

$$E_R^{\text{max}}(E_{\text{el}}) = 2E_{\text{el}} \frac{E_{\text{el}} + 2mc^2}{Mc^2}, \quad (33)$$

which agrees with Eq. (1). Estimates based on this formula suggest that backscattering of electrons with kinetic energies in the MeV range can readily generate atomic recoils with energies many times the magnitude of the potential barrier for vacancy migration in metals.

The characteristic scale of angle  $\theta$  in (31) depends on the differential cross section of scattering. Elastic scattering of relativistic electrons by atoms is well described by

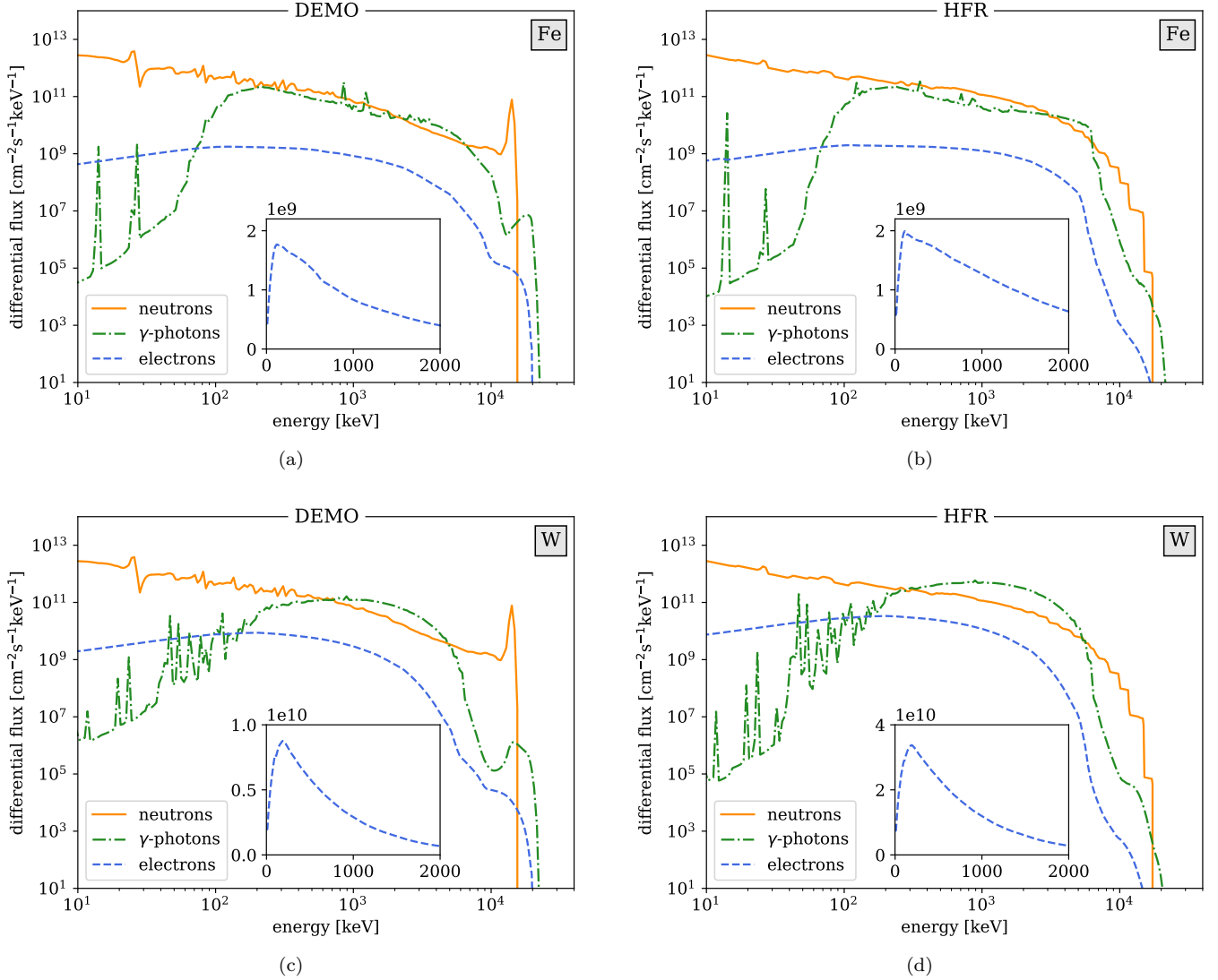


Figure 6. Energy-resolved differential neutron,  $\gamma$ -photon and electron spectra in the bulk of neutron-irradiated Fe (a, b) and W (c, d) corresponding to fusion (DEMO) and fission (HFR) conditions. Insets show the energy-differential electron fluxes on a linear scale. These are all maximum at approximately 200 keV, but even at  $\sim 2$  MeV they still retain  $\sim 10\%$  of the peak intensity. Photon and electron spectra were calculated according to the theory presented in Sec. III.

Table II. Total neutron ( $\Phi_n$ ),  $\gamma$ -photon ( $\Phi_{ph}$ ) and electron ( $\Phi_{el}$ ) fluxes in W and Fe and in DEMO and HFR conditions, calculated as presented in Sec. III, and median particle energy (MNE, MPE and MEE respectively), calculated as the energy below and above which lie the two halves of the total flux.

	$\Phi_n$ [cm <sup>-2</sup> s <sup>-1</sup> ]	MNE [keV]	$\Phi_{ph}$ in W [cm <sup>-2</sup> s <sup>-1</sup> ]	MPE in W [keV]	$\Phi_{ph}$ in Fe [cm <sup>-2</sup> s <sup>-1</sup> ]	MPE in Fe [keV]	$\Phi_{el}$ in W [cm <sup>-2</sup> s <sup>-1</sup> ]	MEE in W [keV]	$\Phi_{el}$ in Fe [cm <sup>-2</sup> s <sup>-1</sup> ]	MEE in Fe [keV]
DEMO	$5.04 \times 10^{14}$	295	$2.74 \times 10^{14}$	1,410	$1.78 \times 10^{14}$	891	$7.57 \times 10^{12}$	589	$2.36 \times 10^{12}$	934
HFR	$6.83 \times 10^{14}$	129	$1.09 \times 10^{15}$	1,480	$2.04 \times 10^{14}$	1,230	$3.03 \times 10^{13}$	589	$3.22 \times 10^{12}$	1,070

the screened Coulomb Rutherford cross section [6, 62, 73]

$$\left(\frac{d\sigma}{d\Omega}\right) = \left(\frac{Ze^2}{4\pi\epsilon_0 mc^2}\right)^2 \left(\frac{1-\beta^2}{\beta^4}\right) \frac{1}{(1+\kappa-\cos\theta)^2}, \quad (34)$$

where  $\beta^2 = v^2/c^2 = 1 - (1 + E/mc^2)^{-2}$ ,  $Z$  is the nuclear

charge, and  $\kappa$  is the screening parameter [62] inversely proportional to the effective size of the atom,

$$\kappa = \frac{\hbar^2}{2p^2 a_{TF}^2}, \quad \kappa \ll 1 \quad (35)$$

where  $p$  is the relativistic momentum of the incident

electron  $p = mv/\sqrt{1 - v^2/c^2}$ , and  $a_{\text{TF}} = 0.885a_B/Z^{1/3}$  is the Thomas-Fermi atomic radius. Here, we use the atomic system of units where the Bohr radius is  $a_B = \hbar^2/me^2 = 0.52918 \text{ \AA}$  and  $e^2/a_B = 27.2116 \text{ eV}$ .

The original Rutherford formula does not treat the effect of screening of the electrostatic potential of the nucleus nor the effects of electron spin. The Mott cross section takes the latter into account by solving the Dirac rather than the Schrödinger equation [74]. The Mott cross section is usually expressed in terms of the Rutherford cross section as

$$\left(\frac{d\sigma_M}{do}\right) = \left(\frac{d\sigma_R}{do}\right) R_M, \quad (36)$$

where factor  $R_M$  for elements with  $Z > 20$  is found numerically [6]. Lijian *et al.* [75] proposed a polynomial interpolation for the unscreened Mott cross section

$$R_M = \sum_{j=0}^4 a_j(Z, \beta)(1 - \cos \theta)^{j/2} \quad (37)$$

where

$$a_j(Z, \beta) = \sum_{k=1}^6 b_{k,j}(Z)(\beta - \bar{\beta})^{k-1}. \quad (38)$$

and  $\bar{\beta} = 0.7181287$ . The numerical values of the coefficients  $b_{k,j}$  can be found in tables [73, 75].

Since the scattering potential is radially symmetric, in the expression for an element of the solid angle  $do$  it is sufficient to retain only the polar component  $do = 2\pi \sin \theta d\theta$ , where  $\theta$  is the angle of scattering of the electron. In the treatment of generation and induced motion of lattice defects, it is convenient to work with the kinetic energy of atomic recoils, related to  $\theta$  by

$$E_R(\theta) = E_R^{\text{max}} \sin^2 \frac{\theta}{2}, \quad (39)$$

which follows from Eqs. (32) and (33). Using the chain rule, we define a quantity

$$\left(\frac{d\sigma}{dE_R}\right) = \left[2\pi \sin \theta \left(\frac{d\sigma}{do}\right)\right]_{\theta=\theta(E_R)} \left|\frac{d\theta}{dE_R}\right|, \quad (40)$$

where

$$\theta(E_R) = 2 \sin^{-1} \sqrt{\frac{E_R}{E_R^{\text{max}}}},$$

$$\left|\frac{d\theta}{dE_R}\right| = \frac{1}{\sqrt{E_R(E_R^{\text{max}} - E_R)}}$$

Similarly to how  $(d\sigma/d\theta)$  gives the probability of an electron being scattered by angle  $\theta$ ,  $(d\sigma/dE_R)$  is proportional to the probability of a target atom receiving recoil energy  $E_R$ .

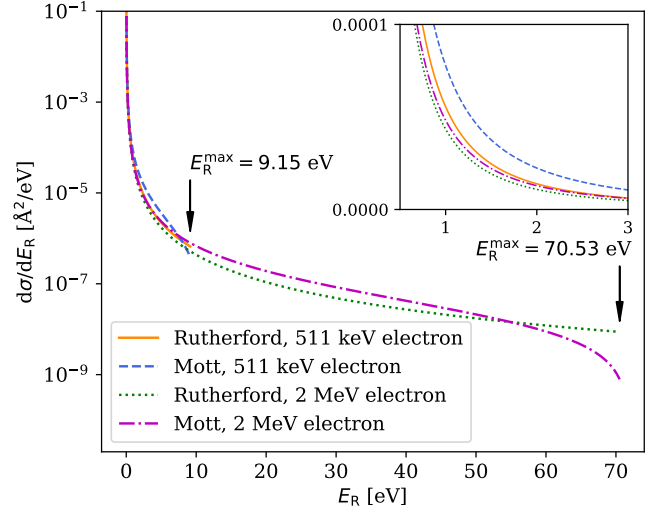


Figure 7. Differential cross sections for a tungsten atom to receive recoil energy  $E_R$  after a collision with an electron with kinetic of 511 keV or 2 MeV, respectively. The screened relativistic Rutherford cross section is compared to the Mott cross section. Both terminate at the maximum recoil energy given by Eq. (1). The inset shows a magnified view of the curve with the vertical axis shown on a linear scale.

Using Eqs. (34) and (36), and noting that

$$\frac{\sin \theta(E_R)}{\sqrt{E_R(E_R^{\text{max}} - E_R)}} = \frac{2}{E_R^{\text{max}}},$$

we simplify Eq. (40) as

$$\left(\frac{d\sigma}{dE_R}\right) = 2\pi \left(\frac{Ze^2}{4\pi\epsilon_0 mc^2}\right)^2 \left(\frac{1 - \beta^2}{\beta^4}\right) \frac{2E_R^{\text{max}}}{(\kappa E_R^{\text{max}} + 2E_R)^2} \quad (41)$$

if scattering is described by the screened relativistic Rutherford cross section. Alternatively,

$$\left(\frac{d\sigma}{dE_R}\right) = 2\pi R_M \left(\frac{Ze^2}{4\pi\epsilon_0 mc^2}\right)^2 \left(\frac{1 - \beta^2}{\beta^4}\right) \frac{E_R^{\text{max}}}{2E_R^2} \quad (42)$$

if scattering is described by the Mott formula. In Fig. 7 we compare the two expressions at two different electron energies. The Mott cross section is more accurate, but computing it requires a large number of coefficients; the Rutherford cross section may be more appropriate since the error that it introduces is small given all the other approximations involved in the analysis.

To validate the method, we now apply Eq. (40) to the evaluation of the rate at which high-energy electrons generate Frenkel pairs (FP) once the transferred recoil energy  $E_R$  surpasses a certain threshold atomic displacement energy barrier [4, 10]. This amounts to estimating the number of stable defects  $N_d(E_R)$  remaining after a collision event. Using the data derived from MD simulations, Yang and Olsson [56] modified the arcpa (athermal recombination-corrected displacement per

atom) model [13] and found that the number of stable defects increases linearly as a function of  $E_R$  above a certain minimum energy  $E_d^{\min}$ . A “defect production differential cross section” can be defined by combining the energy-differential cross section given by Eq. (40) and the Yang-Olsson expression

$$N_d(E_R) = \begin{cases} 0, & E_R < E_d^{\min} \\ \frac{0.8E_R}{2E_d^{\text{avr}}}, & E_d^{\min} < E_R < \frac{2E_d^{\text{avr}}}{0.8} \\ \frac{0.8E_R}{2E_d^{\text{avr}}}\xi(E_R), & E_R > \frac{2E_d^{\text{avr}}}{0.8} \end{cases} \quad (43)$$

where

$$\xi(E_R) = (1 - c_{\text{arc dpa}}) \left( \frac{E_R}{2E_d^{\text{avr}}/0.8} \right)^{b_{\text{arc dpa}}} + c_{\text{arc dpa}}.$$

We then obtain the number of stable defects as a function of recoil energy. The four parameters in Eq. (43) can be obtained by MD simulations, and thus depend on the chosen interatomic potential. For the W potential used in this work, after Ref. [76], we obtained the values:  $E_d^{\min} = 47$  eV,  $E_d^{\text{avr}} = 106$  eV,  $b_{\text{arc dpa}} = -0.80$ ,  $c_{\text{arc dpa}} = 0.23$ . We note that in Eq. (43) we assume that the recoil energy is equal to the damage energy. We are, in other words, neglecting electronic losses because during recoils of energy 10–100 eV only about 5% of the energy is lost to electronic stopping [56].

Since in a single collision any amount of energy  $0 < E_R < E_R^{\max}$  can be transferred, the defect production cross section for a single atom is given by the integral

$$\sigma_{FP} = \int_{E_d^{\min}}^{E_R^{\max}} \left( \frac{d\sigma}{dE_R} \right) N_d(E_R) dE_R. \quad (44)$$

The Frenkel pair production rate per unit volume is proportional to the electron flux  $\phi_{\text{el}}$  and the target atomic density  $n_0$ ,

$$\sim \phi_{\text{el}} n_0 \sigma_{FP}.$$

This appears to suggest that the concentration of Frenkel pairs increases linearly with time, which is approximately valid only at the very early stages of irradiation, where the defects are isolated and do not coalesce or recombine because of elastic interactions, and only if the temperature of the material is sufficiently low so that the thermal diffusion of defects is not activated.

Maury *et al.* [4] measured the variation of electrical resistivity due to the formation of Frenkel pairs in electron-irradiated W at low cryogenic temperatures below 7 K. Assuming that the resistivity increase is proportional to the concentration of Frenkel pairs, in Fig. 8 we compare the data by Maury *et al.* with the results derived from Eq. (44), finding good agreement for the onset of damage — corresponding in our model to a change of slope at  $\sim 1560$  keV — as well as for the shape of the curve with respect to the experimental points.

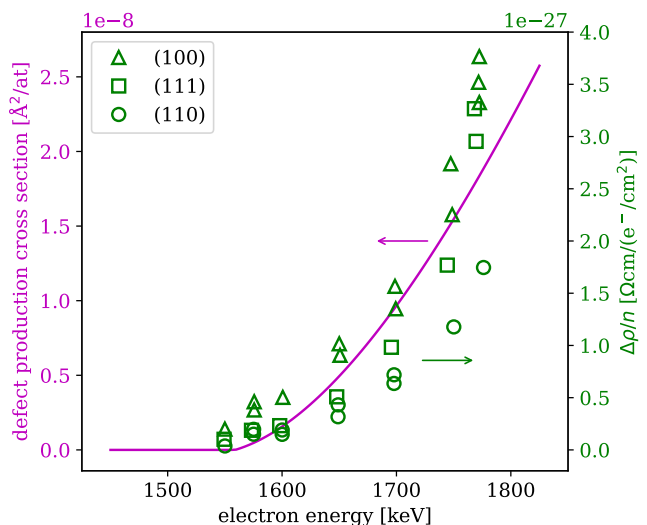


Figure 8. If the maximum recoil energy given by Eq. (1) exceeds the threshold displacement energy, electrons start creating Frenkel pairs that in turn notably increase the electric resistivity of the material [4]. In this figure, we compare the solid line, providing an estimate for the effective cross section of production of Frenkel pairs in W, see text for detail, with experimental results by Maury *et al.* [4].

## V. MOLECULAR DYNAMICS SIMULATIONS

Molecular dynamics simulations of W and Fe were performed using LAMMPS [77] and empirical potentials developed by Mason *et al.* [76] and Gordon *et al.* [78], respectively. A single vacancy was created at the centre of a bcc simulation cell containing 1024 atoms fully relaxed under periodic boundary conditions. The structure was thermalised at a target temperature using a Langevin thermostat with the damping constant of 15.7 ps for W and 0.84 ps for Fe [79]. Electron collisions were simulated by adding a randomly oriented momentum vector  $\mathbf{P}$ , corresponding to a given amount of energy transferred to the atom by an electron, to the instantaneous thermal momentum of the atom. The magnitude of  $P$  was chosen in the way that the energy that the struck atom would have gained in the absence of thermal motion was

$$E_R = \frac{P^2}{2M}.$$

In what follows, we shall demonstrate how thermal vibrations of atoms influence the spectrum of recoil energies caused by high-energy electrons. To see why thermal motion is relevant, let us find the distribution of recoil energies  $f_R(E)$  of atoms that, if at rest, would recoil with  $E_R$ . By adding the transferred momentum to the thermal momentum, see Refs. [67, 68] and Appendix B for detail, we find that the distribution of recoil energies is well approximated by a Gaussian centred at  $E_R$  and with

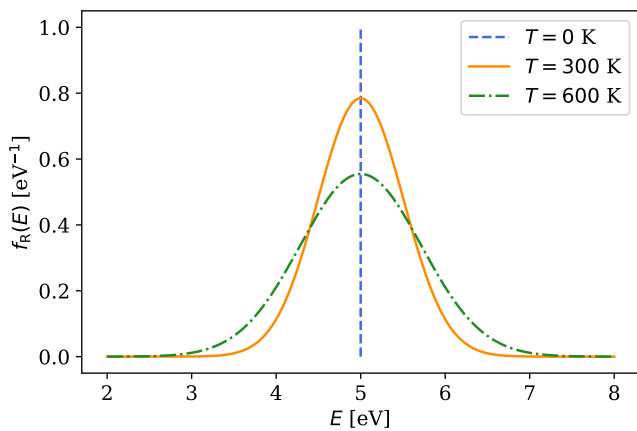


Figure 9. Probability distribution for the energy of recoils  $x$  computed from Eq. (45) assuming that electrons collide with an atom undergoing thermal vibrations at a lattice site. The recoil energy transferred in a collision would be exactly equal to  $E_R = 5$  eV if the atom were at rest. Even if the thermal energy is as low as about 0.05 eV, the broadening of the recoil spectrum is close to 2 eV.

variance  $\sigma^2 = 2(k_B T)E_R$ , namely

$$f_R(E) = \frac{1}{\sqrt{4\pi k_B T E_R}} \exp\left[-\frac{(E - E_R)^2}{4k_B T E_R}\right]. \quad (45)$$

In the above equation,  $k_B$  is the Boltzmann constant. This expression is valid in the limit  $k_B T \ll E_R$ , applicable to the treatment of collisions of atoms with high-energy electrons considered here. We note that although the thermal energy is very small compared to the recoil energy, it has a major effect on the shape of spectrum of atomic recoils [67, 68]. This remarkable manifestation of the Doppler effect is illustrated in Fig. 9.

Simulations were carried out for temperatures  $T = 0, 300, 600,$  and  $900$  K in W, and  $0, 150, 300,$  and  $450$  K in Fe. In relation to Fe, we note that two other potentials, by Mendeleev *et al.* [80] and Malerba *et al.* [81], frequently produce a spurious “split vacancy” defect in near-threshold collisions, see Appendix C. This configuration was very rarely found in the simulations performed using the potential by Gordon *et al.* [78].

We note that although the treatment of collisions with  $\sim$  MeV electrons requires using relativistic mechanics [59], the velocities of atoms receiving recoils are in the non-relativistic  $10^3$  m/s range. 50,000 collisions were simulated at each recoil energy over the energy interval extending up to 10 eV. Depending on the relative orientation of thermal and transferred momenta, the energy of the recoil atom after a collision can be higher or lower than  $E_R$ , as shown in Fig. 9. This is significant, as an electron may collide with an atom moving thermally towards a vacancy, away from it, or at an angle. The total duration of the simulation less than 1  $\mu$ s is such that pure thermally activated hops have a negligible probability. Even at 900 K, a vacancy hops in tungsten on the

timescale of milliseconds, and hence MD simulations performed in this study describe only the mode of diffusion resulting from atomic recoils generated by high-energy electron impacts.

Since collisions with electrons delivering recoil energies in the eV range are quite rare, we simulated them starting each time from a different thermalised configuration. A computational loop was set up as follows: (i) a simulation was run at a constant temperature for 0.310 ps for W and for 0.220 ps for Fe; (ii) the resulting atomic configuration was saved at the end of each run; (iii) a randomly oriented momentum  $\mathbf{P}$  was added to the thermal momentum of an atom in the neighbourhood of a vacancy; (iv) MD simulation was run for 1 ns to give the vacancy a chance to hop to a neighbouring site; (v) simulation was restarted from a configuration saved at step (ii). The time between samplings of initial thermalised configurations was about 12 times the inverse Debye frequency  $\omega_D = k_B T_D / \hbar$ , where  $T_D$  is the Debye temperature, equal to 310 K for W and 410 K for Fe [82], giving  $\omega_D = 4.06 \times 10^{13} \text{ s}^{-1}$  and  $\omega_D = 5.37 \times 10^{13} \text{ s}^{-1}$ , respectively. The sampling frequency ensured that a broad spectrum of initial conditions was explored. As expected, we found that the  $x, y$  and  $z$  components of initial velocities of atoms followed three independent Maxwell-Boltzmann distributions corresponding to the thermalisation temperature.

By recording whether the vacancy had moved after each kick, we found the fraction of successful hops as a function of recoil energy at different temperatures, shown in Fig. 10. A reader will appreciate that, owing to the Doppler effect of Eq. (45), vacancies in Fe or W at a temperature of about 15-25% of the melting point have a finite probability of hopping even when the neighbouring atom recoils with up to about half of the minimum energy that is required to initiate a vacancy hop at 0 K. However, the effect of temperature is no longer significant if the recoil energy is above approximately twice this minimum energy.

## VI. VACANCY DIFFUSION DRIVEN BY HIGH-ENERGY ELECTRONS

We now evaluate the effect of high-energy electron impacts on vacancy diffusion. In a pure material, the thermal part of the vacancy diffusion coefficient  $D$  is [83, 84]

$$D_{\text{th}} = \frac{N_{1\text{NN}}}{6} d^2 \nu_{\text{th}} \exp\left[-\frac{E_a}{k_B T}\right], \quad (46)$$

where  $N_{1\text{NN}}$  is the number of first nearest neighbour (1NN) atoms,  $d$  is the hop distance (if  $a$  is the lattice parameter then  $d = a\sqrt{3}/2$  for bcc and  $d = a\sqrt{2}/2$  for fcc crystals),  $\nu_{\text{th}} = \omega_D/2\pi$  is the thermal attempt frequency, and  $E_a$  is the vacancy migration energy.

In the presence of impurities, the diffusion coefficient can be estimated following Refs. [85, 86]. For example, in Fe and W containing carbon at a concentration exceeding

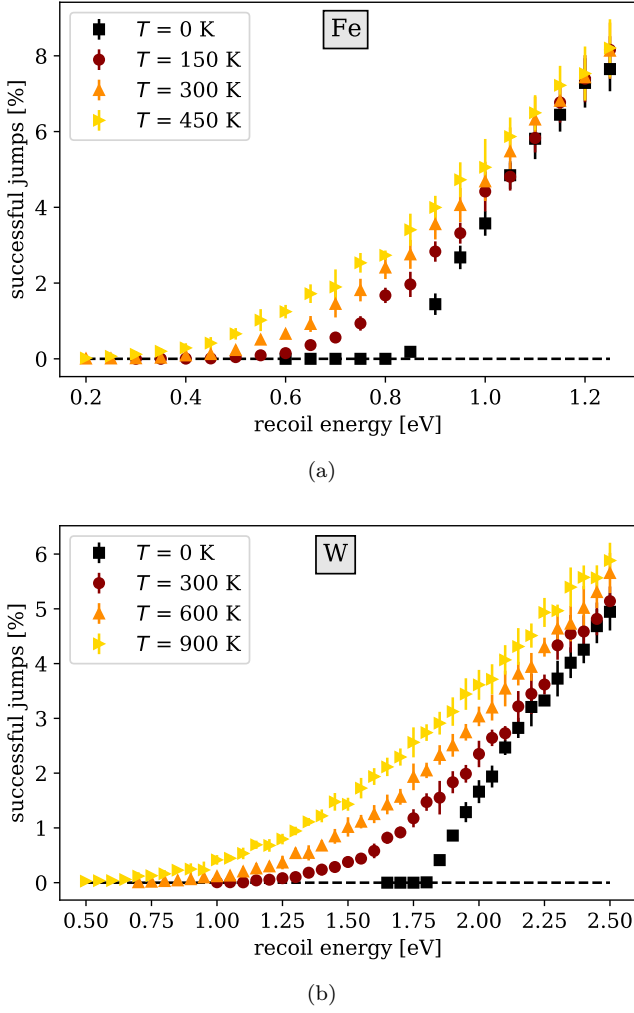


Figure 10. Fraction of atomic recoils resulting in a vacancy hop increases with the amount of energy transferred in a collision, as illustrated by the plots for Fe (a) and W (b). At 0 K, there is a sharp threshold for the reaction. At a finite temperature, thresholds are smooth and vacancy hops occur even at very low recoil energies.

the concentration of vacancies, we find

$$D_{\text{th}}^{\text{C}} = D_{\text{th}} \frac{[V]}{[V_{\text{tot}}]}, \quad (47)$$

where  $[V]$  is the vacancy concentration and  $[V_{\text{tot}}] = [V] + [VC] + [VC_2] + \dots$  is the total concentration of isolated vacancies and carbon-vacancy complexes  $VC_n$ . A single vacancy in Fe and W can trap between one and four C atoms, with the  $VC_2$  complex being the most stable [85–87]. Using the binding energies  $E_n^{\text{b}}$  calculated using density functional theory for Fe [85] and for W [86] we find

$$[VC_n] = [V][C]^n \exp\left(\frac{E_n^{\text{b}}}{k_{\text{B}}T}\right)$$

resulting in

$$D_{\text{th}}^{\text{C}} = \frac{D_{\text{th}}}{1 + \sum_{n=1}^4 [C]^n \exp\left(\frac{E_n^{\text{b}}}{k_{\text{B}}T}\right)}. \quad (48)$$

If atoms are bombarded by high-energy electrons, diffusion is always accelerated, irrespectively of the presence or absence of impurities, by the transfer of kinematic momentum to atoms from electrons. A collision of a high-energy electron with an atom close to a vacancy can stimulate an atomic hop or, equivalently, a vacancy hop to an adjacent lattice site. The threshold energy for a hop depends on the crystallographic direction of the impact and the distance between the atom receiving the impact and a vacancy.

To estimate the contribution of electron impacts to vacancy diffusion, we first need to identify the atoms around a vacancy that could contribute to diffusion through random recoils requiring the least amount of energy to initiate a successful vacancy hop. We simulated, at  $T = 0$  K, the atomic processes initiated by atomic impacts using the interatomic potentials for tungsten by Mason [76] and Marinica [88], and the interatomic potential for iron by Gordon [78]. We considered initial impacts in the  $\langle 111 \rangle$ ,  $\langle 100 \rangle$  and  $\langle 110 \rangle$  directions involving the first, second and third nearest neighbours of a vacancy, and also atoms further away from it.

Table III shows that electron-induced diffusion in W and Fe is dominated by the events involving high-energy electrons colliding with atoms situated along the  $\langle 111 \rangle$  crystallographic directions. In bcc metals there are  $N_{\langle 111 \rangle} = 8$  atoms nearest to a vacancy. The electron collision contribution to the vacancy diffusion coefficient is proportional to the weighted sum of frequencies  $\nu_{\langle 111 \rangle}^{(k)}$  with which one of the atoms at a  $k$ -th position along a  $\langle 111 \rangle$  atomic string causes a vacancy to perform a hop following an event of interaction with a high-energy electron

$$D_{\text{el}} = \frac{N_{\langle 111 \rangle}}{6} d^2 \left( \nu_{\langle 111 \rangle}^{(1)} + \nu_{\langle 111 \rangle}^{(2)} + \dots \right), \quad (49)$$

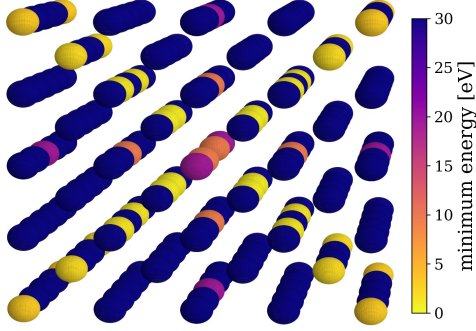
where  $d = a\sqrt{3}/2$  is the nearest neighbour distance between sites in bcc lattice. This provides a lower bound for  $D_{\text{el}}$  as it neglects the events where the struck atom is not situated along a  $\langle 111 \rangle$  atomic string.

To evaluate  $\nu_{\langle 111 \rangle}^{(k)}$ , we note that a vacancy hop to a nearest lattice site involves the following sequence of events

1. an atom near a vacancy is struck by an electron with sufficiently high energy  $E_{\text{el}}$  to initiate a recoil in the eV energy range;
2. the atom recoils in a specific direction with kinetic energy  $E_{\text{R}}$  transferred in the collision with the electron;
3. one of the atoms in the vicinity of a vacancy, not necessarily the atom impacted by the electron,

Table III. Minimum recoil energies resulting in a vacancy hopping to a nearest neighbour position. The values, given in eV units, were computed for  $T = 0$  using two different potentials for W and one for Fe. The atoms receiving the recoils were assumed to be in the first, second, and third NN position in relation to the vacancy. Recoil energy thresholds are visualised for the Mason potential for bcc W [76].

Direction	distance	W [76]	W [88]	Fe [78]
		minimum energy [eV]		
⟨111⟩	1 <sup>st</sup>	1.80	2.23	0.83
	2 <sup>nd</sup>	2.19	3.72	1.25
	3 <sup>rd</sup>	3.03	5.81	1.99
	4 <sup>th</sup>	3.97	8.08	2.87
	5 <sup>th</sup>	4.99	10.3	3.78
	6 <sup>th</sup>	6.06	12.5	4.70
	7 <sup>th</sup>	7.19	14.3	5.59
⟨100⟩	1 <sup>st</sup>	10.1	10.1	4.76
	2 <sup>nd</sup>	19.6	19.1	8.46
	3 <sup>rd</sup>	30.1	28.2	12.7
⟨110⟩	1 <sup>st</sup>	43.3	32.9	17.0



crosses the potential barrier and moves into a stable energy minimum position at the initially vacant lattice site.

Recalling Eq. (3), the *total* frequency of collisions between an atom and electrons depends on the integrated over the solid angle electron flux  $\phi_{\text{el}}(E_{\text{el}})$  defined by (20) and the total cross section of scattering of electrons by an atom  $\sigma_{\text{tot}}(E_{\text{el}})$ ,

$$\nu_{\text{tot}}(E_{\text{el}}) = \phi_{\text{el}}(E_{\text{el}})\sigma_{\text{tot}}(E_{\text{el}}). \quad (50)$$

To account for points 1 and 2 above, we need the frequency *distribution* of atoms as a function of recoil energy  $E_{\text{R}}$ , resulting from collisions with electrons over the entire spectrum of electron energies. The recoil energy-resolved frequency of impact events for an atom at a lattice site is

$$\begin{aligned} \nu(E_{\text{R}}) &= \int d\mathbf{o} \int d\mathbf{o}' \int dE' \frac{d\sigma(\mathbf{n}' \rightarrow \mathbf{n})}{d\mathbf{o}} \phi_{\text{el}}(\mathbf{n}', E') \\ &\times \delta \left\{ E_{\text{R}} - \frac{1}{2} E_{\text{R}}^{\text{max}}(E') [1 - \cos(\mathbf{n} \cdot \mathbf{n}')] \right\}, \quad (51) \end{aligned}$$

where  $E_{\text{R}}^{\text{max}}(E)$  is given by Eq. (33), and  $\delta(x)$  is the Dirac delta function. This equation involves only the

elastic cross section of scattering of electrons by an atom because inelastic scattering of high-energy electrons primarily contributes to energy losses but not to atomic recoils [89]. Integrating (51) over  $E_{\text{R}}$ , we recover expression (50).

If the flux of electrons bombarding the atoms is isotropic, see Eq. (20), in Eq. (51) we integrate over the directions of  $\mathbf{n}'$  and arrive at

$$\begin{aligned} \nu(E_{\text{R}}) &= 2\pi \int_0^\pi d\theta \sin\theta \frac{d\sigma}{d\theta} \int_0^\infty dE \phi_{\text{el}}(E) \\ &\times \delta \left\{ E_{\text{R}} - \frac{1}{2} E_{\text{R}}^{\text{max}}(E) [1 - \cos\theta] \right\}. \quad (52) \end{aligned}$$

Since the angle of scattering  $\theta$  enters Eq. (52) only as an argument of  $\cos\theta$ , we change the variable of integration to  $\xi = 1 - \cos\theta$  and write

$$\begin{aligned} \nu(E_{\text{R}}) &= 2\pi \left( \frac{Ze^2}{4\pi\epsilon_0 mc^2} \right)^2 \int_0^2 d\xi \int_0^\infty dE \phi_{\text{el}}(E) \left( \frac{1 - \beta^2}{\beta^4} \right) \\ &\times \frac{1}{(\kappa + \xi)^2} \delta \left[ E_{\text{R}} - \frac{\xi}{2} E_{\text{R}}^{\text{max}}(E) \right], \quad (53) \end{aligned}$$

where the cross section of scattering is given by the screened Rutherford expression (34). Integrating over  $\xi$ , we find

$$\begin{aligned} \nu(E_{\text{R}}) &= 2\pi \left( \frac{Ze^2}{4\pi\epsilon_0 mc^2} \right)^2 \int_0^\infty dE \phi_{\text{el}}(E) \left( \frac{1 - \beta^2}{\beta^4} \right) \\ &\times \frac{2E_{\text{R}}^{\text{max}}(E)}{[\kappa E_{\text{R}}^{\text{max}}(E) + 2E_{\text{R}}]^2} \Theta [E_{\text{R}}^{\text{max}}(E) - E_{\text{R}}], \quad (54) \end{aligned}$$

where  $\Theta(x)$  is the Heaviside function,  $\Theta(x) = 1$  for  $x > 0$  and  $\Theta(x) = 0$  for  $x < 0$ .

For a mono-energetic flux of electrons with kinetic energy  $\mathcal{E}$ , the expression for the flux has the form  $\phi_{\text{el}}(E) = \Phi_0 \delta(E - \mathcal{E})$  and the distribution of the frequency of atomic recoils with respect to the energy of recoils is

$$\begin{aligned} \nu(E_{\text{R}}) &= 2\pi \left( \frac{Ze^2}{4\pi\epsilon_0 mc^2} \right)^2 \Phi_0 \frac{(1 + \mathcal{E}/mc^2)^2}{[(1 + \mathcal{E}/mc^2)^2 - 1]^2} \\ &\times \frac{2E_{\text{R}}^{\text{max}}(\mathcal{E})}{[\kappa E_{\text{R}}^{\text{max}}(\mathcal{E}) + 2E_{\text{R}}]^2}, \quad (55) \end{aligned}$$

for  $E_{\text{R}} < E_{\text{R}}^{\text{max}}(\mathcal{E})$ . There are no recoils with energies higher than  $E_{\text{R}}^{\text{max}}(\mathcal{E}) = 2\mathcal{E}(\mathcal{E} + 2mc^2)/Mc^2$ .

The same result can be obtained from the energy-differential cross sections, Eq. (41) for the screened Rutherford interaction and Eq. (42) for the Mott scattering, resulting in

$$\nu(E_{\text{R}}) = \int_0^\infty dE_{\text{el}} \phi_{\text{el}} \frac{d\sigma}{dE_{\text{R}}}. \quad (56)$$

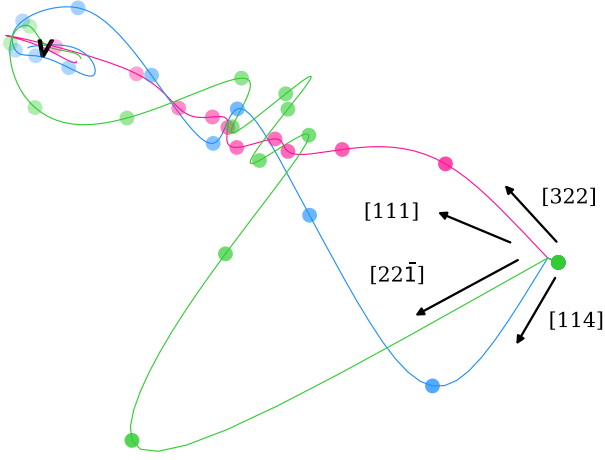


Figure 11. Representative examples of trajectories found in events involving collisions of electrons with atoms in a 1NN shell of a vacancy in W. The [322], [114] and [221] trajectories start at about 11°, 35° and 55° off the [111] crystallographic direction, respectively, and require recoil energies of 2, 5 and 9 eV to enable the atom to successfully complete a hop into a vacant site (marked as V).

In the above equations,  $\nu(E_R)$  is expressed in units  $\text{s}^{-1}\text{eV}^{-1}$  whereas the flux of electrons is expressed in the  $\text{cm}^{-2}\text{s}^{-1}\text{eV}^{-1}$  units.

We now address point 3 above by quantifying the probability of the vacancy hopping to a neighbouring lattice site if a collision with a high-energy electron transfers energy  $E_R$  to one of the neighbouring atoms. This probability, which in what follows we refer to as  $J(E_R, T)$ , depends on the recoil energy and temperature.

Since the spectrum of recoil energies given by Eq. (55) is broad, vacancy hopping events are expected to be dominated by the electron impacts generating recoil energies comparable or greater than the vacancy migration energy. This energy scale is many times the energy of thermal motion of atoms, and hence the statistics of transitions stimulated by electron impacts are expected to be different from the statistics of thermally activated events, detailed in Ref. [90].

The treatment of thermally activated transitions involves computing the rate of a many-body atomic system crossing a potential barrier associated with a reaction where an atom hops to a neighbouring vacant site [90–92]. For thermally activated processes, this rate is exponentially small, and the thermal motion of atoms at equilibrium positions is assumed to be unaffected by the occurrence of transitions.

A typical recoil event stimulated by a high-energy electron collision with an atom has the energy well above the thermal energy but still below the threshold for the formation of a Frenkel pair. The motion of an atom receiving the recoil and its neighbours remains confined to the vicinity of equilibrium positions, although the amplitude of motion is significantly larger than the amplitude of thermal vibrations. The initial energy of the recoil dissi-

pates by phonon radiative transfer. Occasionally, on the timescale of several Debye oscillations, this energy gets partially projected onto the trajectory of a many-body reaction involving a vacancy hopping to a neighbouring lattice site.

Providing an accurate quantitative estimate of  $J(E_R, T)$  is difficult because of the atomic many-body character of recoil-stimulated vacancy hopping events. Trajectories of MD simulations shown in Fig. 11 suggest that the initial direction of an atomic recoil does not have a strong effect on the outcome of a sequence of local interactions between the atoms that eventually result in vacancy migration. Even the recoils at a large angle to the direction of a vacancy hop appear to contribute significantly to the vacancy hopping rate.

At  $T = 0$  K, function  $J(E_R, 0)$  vanishes for all the recoil energies  $E_R < E_a$ , where  $E_a$  is the minimum recoil energy required to initiate a vacancy migration. At a finite temperature,  $J(E_R, T)$  is a monotonically increasing function of  $E_R$ , likely saturating at high recoil energies  $E_R \gg E_a$ , provided that  $E_R$  is still well below the Frenkel pair threshold production energy. MD simulations performed in this study and in Ref. [18] suggest that at high recoil energies function  $J(E_R, T)$  approaches a limit close to 0.27. Notably, this value is higher than the  $1/8 = 0.125$  fraction of the solid angle spanned by the directions from an atom in a corner of a cubic cell towards a vacancy in its centre.

Temperature effects are expected to assist the recoil-stimulated vacancy diffusion. Thermal velocity adds to the velocity of an atom derived from a recoil event if both vectors are aligned towards a vacancy. Also, the effective free-energy migration barrier is lowered by the vibrations of atoms though the entropy effect [93]. A treatment similar to a transition rate theory approach suggests a suitable functional form for  $J(E_R, T)$ , see Appendix D for detail

$$\begin{aligned}
 J(E_R, T) = & \alpha \left( 1 + \frac{1}{2} \left( 1 - \sqrt{\frac{E_a}{E_R}} \right) \operatorname{erf} \left[ \frac{\sqrt{E_R} - \sqrt{E_a}}{\sqrt{k_B T}} \right] \right. \\
 & - \frac{1}{2} \left( 1 + \sqrt{\frac{E_a}{E_R}} \right) \operatorname{erf} \left[ \frac{\sqrt{E_R} + \sqrt{E_a}}{\sqrt{k_B T}} \right] \\
 & \left. + \sqrt{\frac{k_B T}{\pi E_R}} \sinh \left[ \frac{2\sqrt{E_R E_a}}{k_B T} \right] \exp \left[ -\frac{E_a + E_R}{k_B T} \right] \right), \quad (57)
 \end{aligned}$$

where  $\alpha$  is a constant that can be determined from MD simulations. Eq. (57) was derived assuming that the activation energy is the same as in Eq. (46). To account for the entropy term [93], we treat  $E_a$  as a weakly temperature dependent quantity and define

$$E_a(T) = E_a^0 \left( 1 - \frac{T}{T_0} \right), \quad (58)$$

where the constants are material-dependent with  $T_0 \sim 10^4$  K.  $E_a^0$  is the minimum energy required for an atom to hop into a vacant lattice site and it can be derived from a single MD simulation for each of the atoms in

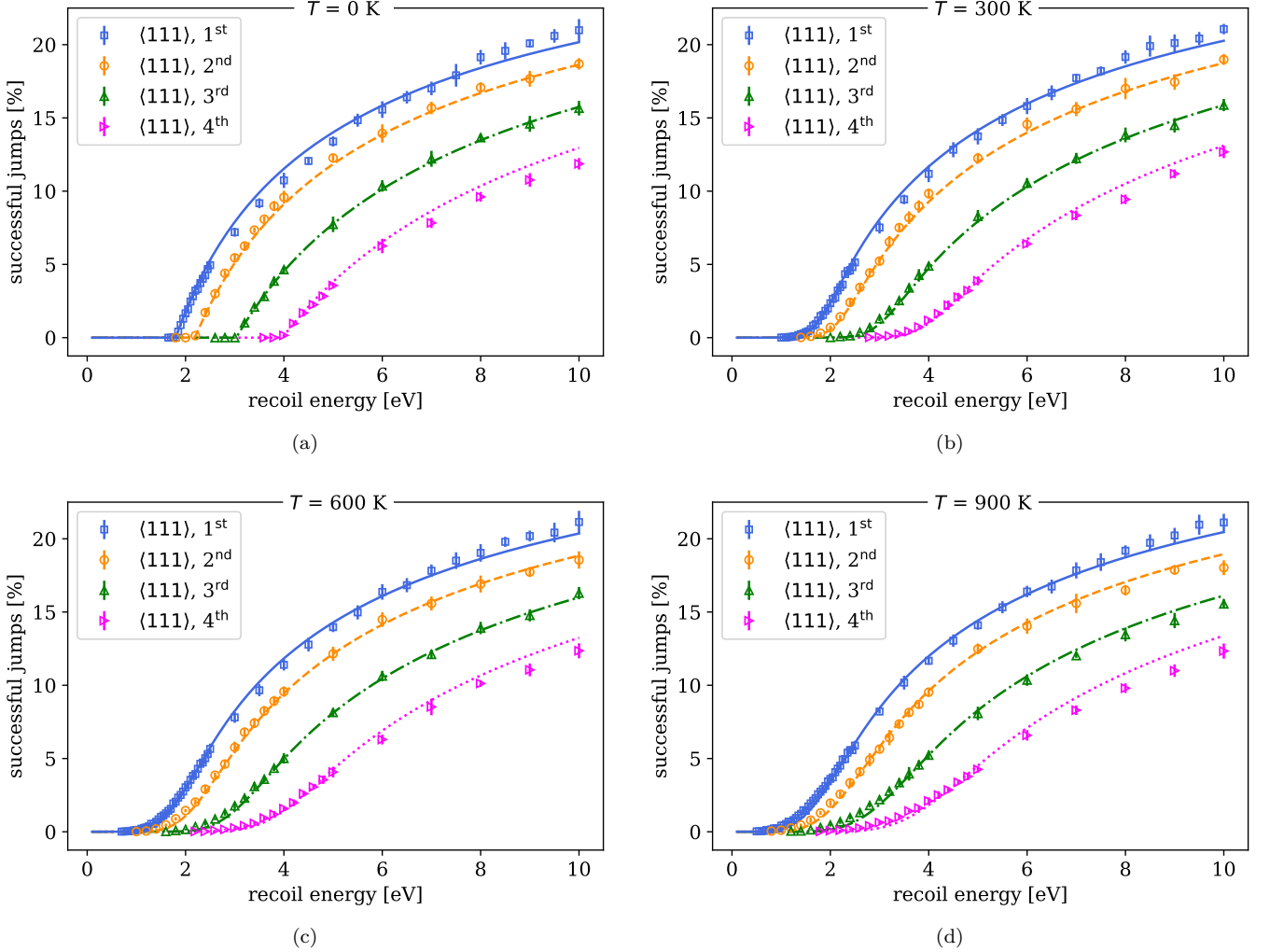


Figure 12. Fraction of successful vacancy hops in W for 0 K (a), 300 K (b), 600 K (c), 900 K (d) if the kicked atom is one of the 1<sup>st</sup>, 2<sup>nd</sup>, 3<sup>rd</sup> or 4<sup>th</sup> atoms along the  $\langle 111 \rangle$  directions. Discrete data points, with error bars indicating one standard deviation, are derived from MD simulations (potential [76]), whereas the fitting curves are given by Eq. (57). Fitting all the data simultaneously yielded a single pair  $\alpha = 0.3504$ ,  $k_B T_0 = 2.038$  eV (with values of  $E_a^0$  in Eq. (58) from Table III). Eq. (57) fits all the data points with  $R^2 = 99.7$  %.

the  $\langle 111 \rangle$  string of atoms, see Table III. As for the choice of parameters  $\alpha$  and  $T_0$ , we found that a single set of two constants is sufficient to fit all of the data derived from extensive MD simulations involving randomly kicking of atoms in the vicinity of a vacancy, at one to four nearest neighbour distances in a  $\langle 111 \rangle$  direction. The MD data and the fits based on the analytical formula Eq. (57) are shown in Fig. 12.

For a given electron flux and resulting distribution of recoil energies, the success rate is given by the product of Eq. (56) and Eq. (57). Since both the electron and recoil energies are given by continuous probability distributions, the total success rate  $\nu_{\langle 111 \rangle}^{(k)}$  is obtained by inte-

grating over all the electron and recoil energies, yielding

$$\nu_{\langle 111 \rangle}^{(k)}(T) = \int_0^\infty dE_{\text{el}} \int_0^\infty dE_{\text{R}} \phi_{\text{el}}(E_{\text{el}}) \frac{d\sigma}{dE_{\text{R}}} J_k(E_{\text{R}}, T). \quad (59)$$

Numerically, the electron flux is represented by a set of  $N$  values  $\Phi_{\text{el}}^{(i)}$  corresponding to discrete electron energies  $E_i$ , and thus the above equation can be written as

$$\phi_{\text{el}}(E_{\text{el}}) = \sum_{n=1}^N \Phi_{\text{el}}^{(i)} \delta(E_{\text{el}} - E_i). \quad (60)$$

Substituting this in Eq. (59) we find that

$$\nu_{\langle 111 \rangle}^{(k)}(T) = \sum_{i=1}^N \int_0^\infty \Phi_{\text{el}}^{(i)} \frac{d\sigma}{dE_{\text{R}}} J_k(E_{\text{R}}, T) dE_{\text{R}}. \quad (61)$$

The  $k$ -th index of  $J_k(E_R, T)$  indicates that the corresponding energy threshold refers to the  $k$ -th atom along the (111) direction. Inserting Eq. (61) into Eq. (49) enables one to calculate  $D_{\text{el}}$ , the high-energy electron recoil contribution to the diffusion of vacancies in a material exposed to neutron irradiation. The barriers listed in Table III were obtained for pure W and Fe. In the presence of C atoms at the vacancy site, we expect them to be higher. We denote by  $D_{\text{el}}^{\text{C}}$  the diffusion coefficient calculated after raising all the minimum hopping energies in Table III.

## VII. VACANCY MIGRATION IN W, STIMULATED BY HIGH-ENERGY ELECTRONS

High-voltage TEM is known to be effective in stimulating vacancy migration in W. We can apply Eq. (49) to evaluate the diffusion coefficient of vacancies stimulated by a flux of  $10^{21} \text{ cm}^{-2}\text{s}^{-1}$  electrons with kinetic energies 200 and 2000 keV [5], as shown in Fig. 13 together with  $D_{\text{th}}$  and  $D_{\text{th}}^{\text{C}}$ . The estimate for  $D_{\text{th}}^{\text{C}}$  is valid in the limit  $[V] \ll [C]$ , i.e. in the case where the accelerating voltage is not sufficient to produce vacancies by electron collisions or, if it is, at the early stages of irradiation. We assume the thermal activation energy of 1.66 eV, and binding energies  $E_n^{\text{b}}$  of 1.93, 1.97, 1.87, 1.54 eV for  $n = 1, 2, 3, 4$  respectively [86]. If the carbon concentration is close to 1 appm,  $D_{\text{th}}^{\text{C}}$  is dominated by the [VC] complexes in the temperature interval between approximately 30 and 1500 K, yielding an Arrhenius behaviour with a pre-exponential factor  $D_0^{\text{C}} = \nu_{\text{th}} a^2 / [C] = 6.55 \times 10^3 \text{ cm}^2/\text{s}$  and an activation energy  $E_a^{\text{C}} = 1.66 + 1.93 = 3.59 \text{ eV}$ . On the basis of this, when calculating  $D_{\text{th}}^{\text{C}}$ , we raised the activation energies entering the four hopping frequencies  $\nu_{\langle 111 \rangle}^{(k)}$  by 1.79 eV to  $E_a = [3.59, 3.98, 4.82, 5.76] \text{ eV}$ .

Conventional thermally activated diffusion exhibits a very strong temperature dependence [90], whereas the temperature dependence is much weaker for the high-energy electron recoil contribution to the vacancy diffusion coefficient. To compare thermal and electron-stimulated contributions to vacancy diffusion, we define the notion of the effective equivalent temperature

$$T_{\text{el}} = \frac{E_a}{k_{\text{B}} \log(D_0/D_{\text{el}})},$$

where  $D_0$ ,  $E_a$  and  $D_{\text{el}}$  depend on whether C impurities are considered or not. At 0 K under electron irradiation, vacancies appear to be as mobile as in pure tungsten at temperatures close to  $T_{\text{el}} = 635$  and 672 K for the two energies of the incident high-energy electrons, respectively. This is fully consistent with experimental observations showing that vacancies were highly mobile under electron irradiation [5]. If 1 appm of C is also present in the material,  $T_{\text{el}}^{\text{C}}$  equals 966 K for the 2 MeV case whereas the electron-driven diffusion is suppressed in the case of 200 keV electrons, because  $E_{\text{R}}^{\text{max}} = 2.85 \text{ eV}$  is lower than the lowest activation energy of 3.59 eV. However, due

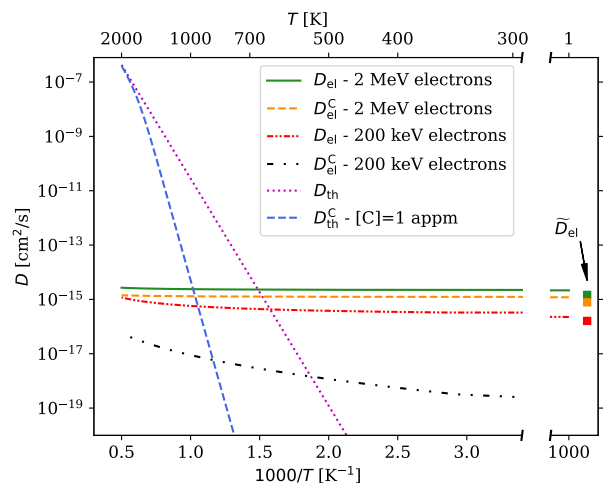


Figure 13. Temperature dependence of electron-stimulated vacancy diffusion in W,  $D_{\text{el}}$ , Eq. (49), compared to thermal diffusion in an ultra-pure,  $D_{\text{th}}$ , Eq. (46), and in C-doped,  $D_{\text{th}}^{\text{C}}$ , Eq. (47), conditions. The effect of carbon is included in  $D_{\text{th}}^{\text{C}}$  by increasing the energies  $E_a^{(k)}$  in Eq. (61) so that the lowest energy matches the C-doped thermal barrier of 3.59 eV. The analysis corresponds to a TEM scenario, with beam energies of 200 keV and 2 MeV and electron flux of  $2 \times 10^{21} \text{ cm}^{-2}\text{s}^{-1}$ . An estimate (63), corresponding to the limiting case for  $1000/T \rightarrow \infty$ , is also shown.  $D_{\text{th}}^{\text{C}}$  for 200 keV electrons vanishes if  $T \rightarrow 0$  as  $E_{\text{R}}^{\text{max}} = 2.85 \text{ eV}$  falls below the raised hopping barrier. Therefore, the electron-driven diffusion observed in this case is entirely due to the Doppler effect.

to the Doppler effect, even if  $T$  is as low as 300 K, the electron-stimulated vacancy diffusion is strong enough to give  $T_{\text{el}}^{\text{C}} = 803 \text{ K}$ . These calculations were performed using the Mott scattering cross section. The Rutherford cross section yields results that are approximately 1.5 times lower but qualitatively consistent with the above estimates.

Eq. (49) enables calculating the vacancy diffusion coefficient and the associated  $T_{\text{el}}$  for a given electron spectrum. We performed this calculation for the two spectra shown in Fig. 6. Table IV compares the computed values with the data for high-voltage TEM electron irradiation, assuming the irradiation temperature of 0 K. Both fission and fusion neutron spectra yield a similar effective temperature for the driven vacancy migration, assuming pure tungsten, of about 135 °C. This temperature is on the lower end of the reported temperature for stage III recovery of neutron-induced damage in W, which is in the range 100–450 °C [94].  $D_{\text{el}}$  in HFR is about four times larger than in DEMO. The effective temperature is significantly higher, and is close to 400 °C, if the effect of 1 appm of carbon is taken into account. However, we note that if under prolonged irradiation the vacancy concentration increases enough so that the fraction trapped by the carbon atoms becomes small, the effect of the carbon-vacancy interaction becomes less noticeable.

Finally, we note that the photons generating the elec-

tron flux in a neutron-irradiated material, in the analysis above are only those generated *internally* by the W nuclei. In the case of a relatively thin W layer like in the current designs of the first wall of a breeding blanket, the *external* photon flux is going to play the dominant part in determine the effective vacancy diffusion temperature.

In W, for the electron energies above hundreds of keV, we find that the correction factor  $R_M$  entering the Mott cross section, the choice of the screening parameter  $\kappa$  in the Rutherford cross section and—most critically—the temperature of the material all have a limited effect on vacancy diffusion. This suggests that it should be possible to derive a simple analytical formula not requiring the numerical integration of Eq. (61). To do this, we take the limit  $\lim_{T \rightarrow 0} J(E_R, T)$  in Eq. (57) and arrive at

$$J(E_R, 0) = \alpha \left( 1 - \sqrt{\frac{E_a}{E_R}} \right) \Theta[E_R - E_a], \quad (62)$$

noting that Eq. (62) sets a lower bound on  $J(E_R, T)$ . Then we set  $\kappa = 0$  in Eq. (34), evaluate the integral in Eq. (61), insert the result into Eq. (49) and find

$$\begin{aligned} \tilde{D}_{\text{el}} = & \frac{\pi\alpha}{3} \left( \frac{Ze^2}{4\pi\epsilon_0 mc^2} \right)^2 \Phi_0 a^2 \left( \frac{1 - \beta^2}{\beta^4} \right) \times \\ & \sum_{k=1}^4 \left[ \frac{E_R^{\text{max}}}{E_a^{(k)}} + 2\sqrt{\frac{E_a^{(k)}}{E_R^{\text{max}}}} - 3 \right]. \end{aligned} \quad (63)$$

This equation is valid if  $E_R^{\text{max}} > E_a^{(k)}$ , whereas  $\tilde{D}_{\text{el}} = 0$  otherwise.

We considered the mono-energetic electron beam case ( $N = 1$  in Eq. (61)) and we considered only the first four atoms along the  $\langle 111 \rangle$  directions as contributing to the recoil-stimulated diffusion. For W, the activation energies are  $E_a = [1.80, 2.19, 3.03, 3.97]$  eV, see Table III. This formula provides a simple but accurate estimate of the effective temperature of a W sample in a TEM given the accelerating voltage and the electron flux. The value yielded by Eq. (63) is shown in Fig. 13 next to the corresponding curve obtained by direct numerical integration. The difference with respect to the right-most point of the curves, i.e.  $T = 1$  K, is a factor of about 1.5, which is entirely due to the ratio between the Mott and the Rutherford cross sections. Taking as an example a 2000 kV TEM scenario where the  $\Phi_{\text{el}} = 2 \times 10^{21} \text{ cm}^{-2}\text{s}^{-1}$  and  $T = 300$  K, we find that  $D_{\text{el}} = 2.22 \times 10^{-15} \text{ cm}^2/\text{s}$  if the estimate involves using the Mott cross section and  $1.52 \times 10^{-15} \text{ cm}^2/\text{s}$  if the Rutherford cross section is used. The corresponding value derived directly from Eq. (63), hence at 0 K, is in this case  $1.46 \times 10^{-15} \text{ cm}^2/\text{s}$ .

### VIII. CONCLUSIONS

Neutron irradiation deposits energy in materials through a variety of nuclear interactions; these include

Table IV. Diffusion coefficient of vacancies in W resulting from exposure to high-energy electrons. Parameters for the high-voltage TEM (HVTEM) electron irradiation, the accelerating voltage of 2 MV and the lower and upper values of flux of electrons, were taken from Ref. [5]. The Mott cross section was used in the calculations.

	$D_{\text{el}}$ [cm <sup>2</sup> /s]	$T_{\text{el}}$ [K]	$D_{\text{el}}^{\text{C}}$ [cm <sup>2</sup> /s]	$T_{\text{el}}^{\text{C}}$ [K]
DEMO	$4.88 \times 10^{-24}$	396	$1.84 \times 10^{-24}$	657
HFR	$1.99 \times 10^{-23}$	408	$7.55 \times 10^{-24}$	672
HVTEM ( $2 \times 10^{21} \text{ cm}^{-2}\text{s}^{-1}$ )	$2.15 \times 10^{-15}$	672	$1.20 \times 10^{-15}$	966
HVTEM ( $5 \times 10^{18} \text{ cm}^{-2}\text{s}^{-1}$ )	$5.38 \times 10^{-18}$	556	$3.00 \times 10^{-18}$	848

elastic and inelastic collisions with atomic nuclei and non-elastic interactions such as neutron capture or multiplication. The resulting nuclei are left in internally excited states that emit  $\gamma$ -photons as they decay. The fraction of energy of neutrons converted into a flux of  $\gamma$ -photons strongly depends on the elemental content of the material. For example, in W the proportion of kinetic energy of neutrons converted into electromagnetic  $\gamma$ -radiation approaches 99 %, which is higher than the light generation efficiency of LED devices, whereas in Be this fraction is less than 1 %, assuming exposure to identical neutron spectra.

The energetic secondary  $\gamma$ -photons play a significant part in the microstructural evolution of W exposed to neutron irradiation. In a two-step process, neutrons generate  $\gamma$ -photons that in turn excite high-energy electrons in the material. Starting from an energy-resolved neutron spectrum, we compute the energy-resolved  $\gamma$ -photon and electron spectra. In W and Fe, the DEMO fusion and HFR fission neutrons produce the  $\gamma$ -photon and electron spectra that have energies in the range from hundreds of keV to several MeV. These high-energy electrons have sufficient energy to stimulate athermal migration of vacancies and other defects through relatively low energy atomic recoils, which on their own do not produce radiation defects. The frequency of vacancy hops stimulated by interaction with electrons depends on the energy-differential atomic cross section and many-body atomic transitions triggered by the recoils. A functional form for the athermal diffusion coefficient is confirmed by molecular dynamics simulations. The results highlight the role of the Doppler effect in lowering the threshold energy for vacancy migration.

The diffusion coefficient for electron-stimulated diffusion in W is evaluated assuming DEMO, HFR and high-voltage TEM irradiation exposure. In a neutron field, even if W is assumed to be at very low temperature, vacancies are as mobile as if, in the absence of impurities, the temperature were close to 400 K. This effective temperature is even higher if we take into account the interaction of vacancies with impurities, for example carbon. Since the process of electron-driven vacancy diffu-

sion is entirely athermal, no cooling of the material can deactivate this neutron-photon-electron mode of diffusion stimulated by irradiation. Atomic recoils initiated by the high-energy electrons, produced by the  $\gamma$ -quanta resulting from the neutron-stimulated nuclear excitations, have a broad energy spectrum extending into the several eV range even in tungsten, and hence the same mechanism likely stimulates a variety of other reactions between the defects involving high activation energies.

## ACKNOWLEDGMENTS

The authors would like to thank M. Rieth, D. Terentyev, S. Kalcheva, and G. Pintsuk for stimulating discussions. This work has been carried out within the framework of the EUROfusion Consortium, funded by the European Union via the Euratom Research and Training Programme (Grant Agreement No 101052200 — EUROfusion) and from the EPSRC Energy Programme (grant number EP/W006839/1). To obtain further information on the data and models underlying the paper please contact PublicationsManager@ukaea.uk. Views and opinions expressed are however those of the authors only and do not necessarily reflect those of the European Union or the European Commission. Neither the European Union nor the European Commission can be held responsible for them. We gratefully acknowledge the provision of computing resources by the IRIS (STFC) Consortium.

### Appendix A: The total cross section of Compton scattering

The kernel of Eq. (12) is the energy-differential cross section involving only the Compton scattering of photons. This cross section describes scattering of a photon with the initial energy  $E'$  into a state with any energy between  $E'$  and  $E'/(1 + 2E'/mc^2)$ . Therefore, the total Compton scattering cross section in Eq. (19), tabulated in Ref. [60], can also be found by integrating Eq. (12) over all the energies  $E$  after scattering

$$\begin{aligned} \tilde{\sigma}_{\text{CS}}(E') &= \int dE \int d\Omega' \frac{d^2\sigma(\mathbf{n}', E' \rightarrow \mathbf{n}, E)}{d\Omega' dE'} \quad (\text{A1}) \\ &= \int dE K(E, E'). \end{aligned}$$

By integrating Eq. (12) over the interval of energies  $E'/(1 + 2E'/mc^2) < E < E'$  we find that

$$\begin{aligned} \tilde{\sigma}_{\text{CS}}(\varepsilon) &= 2\pi r_c^2 \left[ \frac{2}{\varepsilon^2} + \frac{(\varepsilon + 1)}{(2\varepsilon + 1)^2} + \frac{\log(1 + 2\varepsilon)}{2\varepsilon} \right. \\ &\quad \left. - \frac{2(\varepsilon + 1)}{\varepsilon^3} \tanh^{-1} \left( \frac{\varepsilon}{\varepsilon + 1} \right) \right], \quad (\text{A2}) \end{aligned}$$

where  $\varepsilon = E'/mc^2$ .

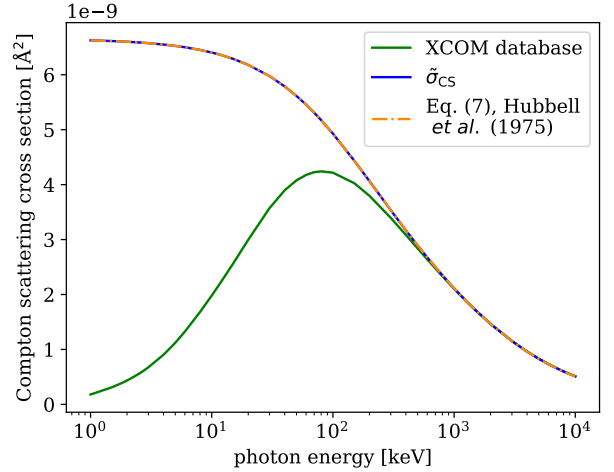


Figure 14. Total Compton cross section of scattering for a single electron, obtained by integrating the Klein-Nishina cross section (blue), is compared with the data available in the XCOM database for W [29] (green) and analytical expression from Ref. [60]. The assumption that even electrons in the inner shells of atoms act as independent scattering centres is very accurate if the photon energy exceeds  $\sim 300$  keV.

Comparison of Eq. (A2) and  $\sigma_{\text{CS}}$  from [29] is given in Fig. 14. Eq. (7) of Ref. [60] provides a different expression for Eq. (A2), which is also included in the figure. We see that for energies of interest of  $\sim 300$  keV and above, the assumption that there are  $Z/\omega$  independent electrons, where  $\omega$  is the atomic volume, is very accurate. At 100 keV Eq. (A2) overestimates the data from [29] by only 16%.

### Appendix B: Thermal broadening of recoil energy

Consider a collision between a high-energy electron and an atom. If the latter is at rest, it recoils with velocity  $(v_{x,R}, v_{y,R}, v_{z,R})$  and kinetic energy  $E = E_R = \frac{m}{2}(v_{x,R}^2 + v_{y,R}^2 + v_{z,R}^2)$ . If the atom also had some initial thermal velocity  $(v_{x,T}, v_{y,T}, v_{z,T})$ , the kinetic energy  $E$  after the collision is

$$E = \frac{m}{2}v^2 = E_T + E_{\text{mix}} + E_R, \quad (\text{B1})$$

namely the sum of the thermal energy  $E_T = m/2(v_{x,T}^2 + v_{y,T}^2 + v_{z,T}^2)$ , the athermal recoil energy  $E_R$ , and a mixing term

$$E_{\text{mix}} = m(v_{x,T}v_{x,R} + v_{y,T}v_{y,R} + v_{z,T}v_{z,R}). \quad (\text{B2})$$

At  $T > 0$ , the atom may receive more or less energy than it would at absolute zero, enabling collisions below the threshold to provide sufficient energy to cause a transition. The distribution of energy  $E$  depends on the distribution of the individual terms, one of which is a constant  $E_R$ .

$E_T$  follows the Maxwell-Boltzmann distribution for a particle of mass  $m$  at temperature  $T$ .  $E_{\text{mix}}$  is the sum of three independent terms, where each is a product of thermal velocity that obeys a 1D Maxwell-Boltzmann distribution, i.e. a Gaussian distribution, and a term that is uniformly distributed between two extrema  $\pm\sqrt{2E_R/m}$ . It can be shown that  $E_{\text{mix}}$  follows a Gaussian distribution whose mean is zero and whose standard deviation is  $\sigma = \sqrt{2k_B T E_R}$ . For the simulations that we considered,  $E_R$  is of the order of 1-10 eV, whereas  $k_B T$  is of the order of 0.03-0.08 eV. Hence, the distribution of  $E$  is primarily that of  $E_R + E_{\text{mix}}$ , i.e. Eq. (45)

$$f_R(E) = \frac{1}{\sqrt{4\pi k_B T E_R}} \exp\left[-\frac{(E - E_R)^2}{4k_B T E_R}\right], \quad (\text{B3})$$

plus a correction given by the thermal contribution  $E_T$ , which is not trivial to evaluate as  $E_{\text{mix}}$  and  $E_T$  are not independent. However, this correction is of second-order if  $k_B T \ll E_R$ . We note that the effect of temperature on the kinetic energy after the collision does not depend on the thermal energy  $k_B T$ , but rather on  $\sqrt{(k_B T)E_R}$ , and therefore can be much greater than what one might anticipate from some simple energy addition argument [67, 68].

### Appendix C: Interatomic potential for Fe

The energy landscape that an atom experiences when hopping into a vacancy, treated as a function of reaction coordinate, may have local minima. If this happens, the atom can get stuck in one of these minima. We found that this commonly occurs in Fe, but does not happen in W. The local minimum corresponds to a ‘‘split vacancy’’ defect, where the Fe atom finds itself in a stable position between two neighbouring lattice sites, which both can be identified as vacancies. For this to happen, the atom must arrive at the midpoint between the two lattice sites with a low kinetic energy. The depth of the local minimum depends on the potential. As this local minimum is an artifact of parameterization of the potential, we selected a potential where this minimum is as shallow as possible. To this end, we tested three different potentials, namely by Mendeleev *et al.* [80], Malerba *et al.* [81], and Gordon *et al.* [78].

Consider the simple case where one of the first nearest neighbours of the vacancy receives a kick precisely along the (111) direction towards the vacancy, at 0 K. If using the Mendeleev potential, a split vacancy remains stable after kicks in the recoil energy range from 0.9-1.05 eV, while the hop is not successful if the recoil energy is 0.85 eV and successful if it is above 1.1 eV. Similarly, the Malerba potential predicts a split vacancy for the recoil energies between 1.05-1.15 eV, an unsuccessful hop at 1.0 eV and a full hop at 1.2 eV. On the other hand, with the Gordon potential an attempt is unsuccessful at 0 K if the recoil energy is 0.81 eV and is fully successful if it is 0.83 eV,

with a much more narrowly-defined activation energy of 0.82 eV.

The influence of the intermediate local minimum on the results is very strong. Fig. 15 shows histograms of the displacement experienced by the 1NN between the beginning and the end of 20,000 recoils in random directions with various energies and at different temperatures. The two expected outcomes for the displacement are either approximately null (if the attempt is unsuccessful), or approximately  $\sqrt{3}a/2 \approx 2.48 \text{ \AA}$  (if the attempt is successful), with possibly a spread due to thermal vibrations. In the top row of Fig. 15, produced using the potential by Mendeleev *et al.*, one can clearly appreciate the presence of a third cluster of realisations, where the atom is stuck in the middle of the hop. This undesirable third outcome is substantially more likely than the full hop if the recoil energy is close to the vacancy migration energy. On the other hand, the same simulations repeated with the potential by Gordon *et al.* show that half-hops are very unlikely at 0 K and never occur at 300 K.

Fig. 16 shows the effect of the choice of potential on the fraction of successful hops for the same potentials and for different temperatures. The presence of half hops fundamentally alters the results for the Mendeleev potential, but has a negligible effect for the Gordon potential. For the results, and for Fig. 10, the very few instances of half hops that were found at 0 K were equally divided between successful and unsuccessful outcomes.

### Appendix D: Probability function of successful hops: Eq. (57)

In order to relate electron-induced recoils and vacancy diffusion, one has to quantify the probability that a collision of an electron with a random atom in a random direction leads to a vacancy hopping by one or more lattice spacing. We assume that this function  $J(E_R)$  is a function of the recoil energy only. The electron flux  $\phi_{\text{el}}(\mathbf{n}, E_{\text{el}})$  is assumed to be isotropic and thus solely a function of the electron energy because the  $\gamma$ -photons that are generated by nonelastic neutron reactions are emitted in a random direction and have long attenuation distance of the order of a cm before they generate high energy electrons that in turn are excited in a random directions. We present a semi-analytical model to predict  $J(E_R)$ , and verify the model by MD simulations, which are also used to parameterise the analytical result.

Assuming the vacancy as a quasi-particle moving in a one-dimensional potential energy landscape, we start from a one-dimensional Langevin equation for a particle of mass  $m$  and friction coefficient  $\gamma$ ,

$$m \frac{\partial^2 x}{\partial t^2} = -\frac{\partial V(x)}{\partial x} - \gamma \frac{\partial x}{\partial t} + \eta(x, t). \quad (\text{D1})$$

The particle moves in a potential that we assume for

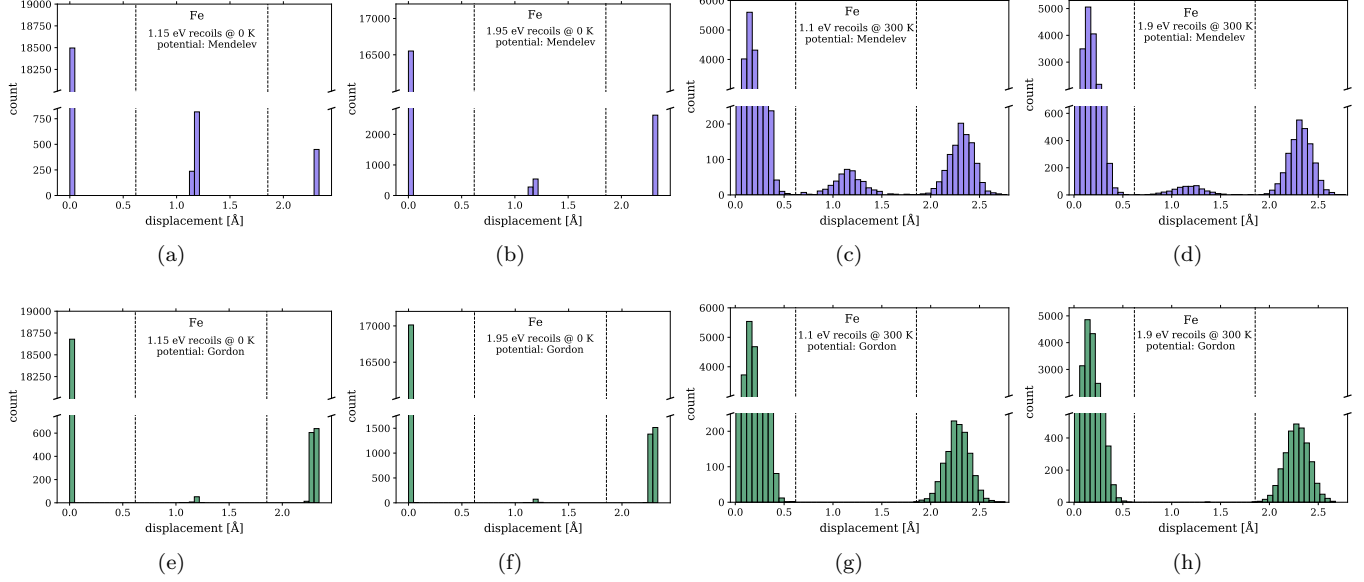


Figure 15. Histograms showing distributions of displacements of 1NN hops after recoils in random directions simulated at 0 K and at 300 K. Displacement is defined as the distance between the coordinate of the atom at the beginning and the end of each realisation. The most likely outcome is that the atom returns to the initial position. Successful hops form the distributions centred at  $\approx 2.48 \text{ \AA}$ . The instances of formation of “split vacancy” configurations are responsible for the distributions shown in the centre. The split vacancy configuration forms much more often with the Mendelev potential (a-d) than with the Gordon potential (e-h).

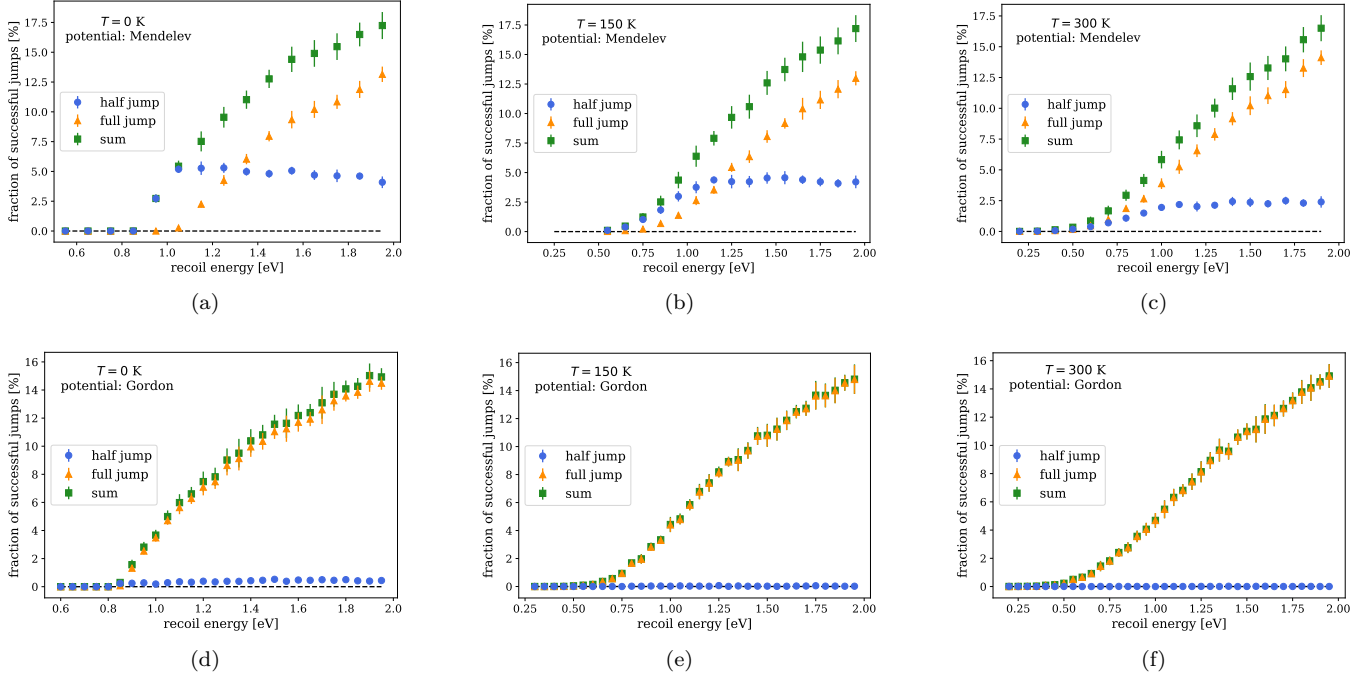


Figure 16. Fraction of successful hops in Fe plotted for the Mendelev (a-c) and Gordon (d-f) potentials, similarly to Fig. 10. For the former potential, the instances of half hop are comparable in the frequency of occurrence to those of complete hops, and are dominant for the recoil energies close to the top of the migration barrier. For the latter potential, the occurrence of half hops is very unlikely and only detectable at 0 K.

simplicity to be

$$V(x) = E_a \sin^2 \left( \frac{\pi x}{\lambda} \right), \quad (\text{D2})$$

with the periodicity of  $\lambda = \frac{\sqrt{3}}{2}a$  in a bcc crystal.  $\eta(x, t)$  is a stochastic force that satisfies the so-called white noise conditions

$$\langle \eta(x, t) \rangle = 0 \quad (\text{D3})$$

$$\langle \eta(x, t) \eta(x', t') \rangle = 2k_B T \gamma \delta(x - x') \delta(t - t'), \quad (\text{D4})$$

i.e. it has zero mean and is uncorrelated in space and time.

The particle initially is at  $x_0$  and has velocity  $v_0$ . At  $t = 0$ , it receives a recoil so that the velocity becomes

$$v = v_0 + v_R,$$

where  $v_R = \sqrt{2E_R/m}$  is defined at 0 K. We assume that the influence of stochastic force and friction are both negligible. The former gives rise to thermal fluctuations on the energy scale about 10–100 times lower than  $E_R$ . The latter is weak on the time scale  $\sim 1$  ns of the transition. For a vacancy to migrate, the kinetic energy after the recoil must be above the barrier height

$$\frac{1}{2}mv^2 > E_a - V(x_0).$$

If the temperature is low, we assume that  $E_a - V(x_0) \approx E_a$ , leading to the condition

$$v^2 > \frac{2E_a}{m}. \quad (\text{D5})$$

To find the likelihood of this condition being met, we need to know the probability distribution function (PDF) for  $v^2$ . In a 1D problem, the thermal part is a Gaussian

distribution  $f_{v_0}(v)$  with zero mean and the standard deviation of  $\sigma = k_B T/m$ . Contribution from collisions  $v_R$  is drawn from the uniform distribution

$$f_{v_R}(v) = \begin{cases} \frac{1}{2v_R}, & |v| < v_R \\ 0, & \text{otherwise,} \end{cases}$$

as this generates recoils with random orientations in 3D. The PDF for the sum of the two is given by their convolution

$$\begin{aligned} f_v(v) &= \int_{-\infty}^{\infty} dv' f_{v_0}(v - v') f_{v_R}(v') \\ &= \frac{1}{4v_R} \left[ \operatorname{erf} \left( \frac{v + v_R}{\sqrt{2}\sigma} \right) - \operatorname{erf} \left( \frac{v - v_R}{\sqrt{2}\sigma} \right) \right]. \end{aligned} \quad (\text{D6})$$

The PDF of  $v^2$  follows from Eq. (D6) through a change of variable  $g(y) = y^2$  with  $y = v^2$ . From

$$f_y(y) = f_v(g^{-1}(y)) \left| \frac{d(g^{-1}(y))}{dy} \right|, \quad (\text{D7})$$

we find

$$f_{v^2}(v^2) = \frac{1}{4v_R \sqrt{v^2}} \left[ \operatorname{erf} \left( \frac{\sqrt{v^2} + v_R}{\sqrt{2}\sigma} \right) - \operatorname{erf} \left( \frac{\sqrt{v^2} - v_R}{\sqrt{2}\sigma} \right) \right]. \quad (\text{D8})$$

The probability of a successful hop  $p(v^2 > \frac{2E_a}{m})$  follows as

$$\begin{aligned} p \left( v^2 > \frac{2E_a}{m} \right) &= \frac{1}{2} \int_{2E_a/m}^{\infty} ds f_{v^2}(s) \\ &= \frac{1}{2} + \frac{1}{4} \left( 1 - \sqrt{\frac{E_a}{E_R}} \right) \operatorname{erf} \left[ \frac{\sqrt{E_R} - \sqrt{E_a}}{\sqrt{k_B T}} \right] \\ &\quad - \frac{1}{4} \left( 1 + \sqrt{\frac{E_a}{E_R}} \right) \operatorname{erf} \left[ \frac{\sqrt{E_R} + \sqrt{E_a}}{\sqrt{k_B T}} \right] \\ &\quad + \sqrt{\frac{k_B T}{4\pi E_R}} \sinh \left[ \frac{2\sqrt{E_R E_a}}{k_B T} \right] \exp \left[ -\frac{E_a - E_R}{k_B T} \right], \end{aligned} \quad (\text{D9})$$

where the factor of 1/2 in front of the integral indicates that the kick can be given either towards or away from the vacancy. We assume that the 1D approximation adequately describes a reaction along a one-dimensional reaction pathway, and that the 3D atomic dynamics alters the result only through an extra scaling factor that we call  $\alpha$ . This leads to the functional form  $J(E_R, T)$  for the transition probability given by Eq. (57).

[1] L. Reali, M. Boleininger, M. R. Gilbert, and S. L. Dudarev, Macroscopic elastic stress and strain produced by irradiation, *Nucl. Fusion* **62**, 016002 (2022).

[2] M. Abdou and C. Maynard, Computational methods for nuclear heating-part ii: Applications to fusion-reactor blankets and shields, *Nucl. Sci. Eng.* **56**, 381 (1975).

- [3] C. B. Lushchik, I. K. Vitol, and M. A. Élango, Decay of electronic excitations into radiation defects in ionic crystals, *Sov. Phys. Usp.* **20**, 489 (1977).
- [4] F. Maury, M. Biget, P. Vajda, A. Lucasson, and P. Lucasson, Frenkel pair creation and stage I recovery in W crystals irradiated near threshold, *Radiat. Eff.* **38**, 53 (1978).
- [5] K. Arakawa, M.-C. Marinica, S. Fitzgerald, L. Proville, D. Nguyen-Manh, S. L. Dudarev, P.-W. Ma, T. D. Swinburne, A. M. Goryaeva, T. Yamada, T. Amino, S. Arai, Y. Yamamoto, K. Higuchi, N. Tanaka, H. Yasuda, T. Yasuda, and H. Mori, Quantum de-trapping and transport of heavy defects in tungsten, *Nature Mater.* **19**, 508 (2020).
- [6] L. Reimer, *Transmission Electron Microscopy* (Springer, Berlin, 1984) Chap. 5, p. 135.
- [7] M. Griffiths, R. C. Styles, C. H. Woo, F. Phillipp, and W. Frank, Study of point defect mobilities in zirconium during electron irradiation in a high-voltage electron microscope, *J. Nucl. Mater.* **208**, 324 (1994).
- [8] G. S. Was, Z. Jiao, E. Getto, K. Sun, A. M. Monterrosa, S. A. Maloy, O. Anderoglu, B. H. Sencer, and M. Hackett, Emulation of reactor irradiation damage using ion beams, *Scripta Mater.* **88**, 33 (2014).
- [9] G. S. Was and S. J. Zinkle, Toward the use of ion irradiation to predict reactor irradiation effects, in *Comprehensive Nucl. Mater.*, Vol. 1, edited by R. J. M. Konings and R. E. Stoller (Elsevier, 2020) 2nd ed., pp. 468–484.
- [10] P. Vajda, Anisotropy of electron radiation damage in metal crystals, *Rev. Mod. Phys.* **49**, 481 (1977).
- [11] J. A. Dicarolo and J. T. Stanley, Energy dependence of electron-induced radiation damage in tungsten, *Radiat. Eff.* **10**, 259 (1971).
- [12] Q. Xu, T. Yoshiie, and H. Huang, Molecular dynamics simulation of vacancy diffusion in tungsten induced by irradiation, *Nucl. Instrum. Methods Phys. Res. Sect. B* **206**, 123 (2003).
- [13] K. Nordlund, S. J. Zinkle, A. E. Sand, F. Granberg, R. S. Averback, R. Stoller, T. Suzudo, L. Malerba, F. Banhart, W. J. Weber, *et al.*, Improving atomic displacement and replacement calculations with physically realistic damage models, *Nature Commun.* **9**, 1 (2018).
- [14] D. Nguyen-Manh, A. Horsfield, and S. Dudarev, Self-interstitial atom defects in bcc transition metals: Group-specific trends, *Phys. Rev. B* **73**, 020101 (2006).
- [15] K. Urban and A. Seeger, Radiation-induced diffusion of point-defects during low-temperature electron irradiation, *Philos. Mag.* **30**, 1395 (1974).
- [16] Y. Satoh, H. Abe, and T. Matsunaga, Radiation-induced glide motion of interstitial clusters in concentrated alloys, *Philos. Mag.* **94**, 2170 (2014).
- [17] H. Jiang, L. He, D. Morgan, P. M. Voyles, and I. Szlufarska, Radiation-induced mobility of small defect clusters in covalent materials, *Phys. Rev. B* **94**, 024107 (2016).
- [18] Y. Satoh, T. Sohtome, H. Abe, Y. Matsukawa, and S. Kano, Athermal migration of vacancies in iron and copper induced by electron irradiation, *Philos. Mag.* **97**, 638 (2017).
- [19] G. F. Knoll, *Radiation Detection and Measurement*, 4th ed. (John Wiley & Sons, US, 2010).
- [20] K. S. Krane, *Introductory Nuclear Physics*, 2nd ed. (John Wiley & Sons, US, 1988).
- [21] J. Jeet, A. B. Zylstra, M. Rubery, Y. Kim, K. D. Meaney, C. Forrest, V. Glebov, C. J. Horsfield, A. M. McEvoy, and H. W. Herrmann, Inertial-confinement fusion-plasma-based cross-calibration of the deuterium-tritium  $\gamma$ -to-neutron branching ratio, *Phys. Rev. C* **104**, 054611 (2021).
- [22] H. Matsunobu and N. Yamamuro, Evaluation of the Nuclear Data on  $(\alpha, n)$  Reaction for F, Na, Al, Cr, Fe, Ni, and Cu, *J. Nucl. Sci. Technol.* **39**, 188 (2002).
- [23] Aydin, Abdullah, Yildiz, Ercan, and Sarpün, Ismail Hakki, Theoretical investigation of cross sections and astrophysical S-factors for the  $^{92}\text{Mo}(\alpha, n)^{95}\text{Ru}$  and  $^{94}\text{Mo}(\alpha, n)^{97}\text{Ru}$  reactions, *EPJ Web Conf.* **128**, 01004 (2016).
- [24] Yildiz, Ercan, The  $(\alpha, n)$  reaction cross-section calculations for some isotopes of iron group elements in the range of 5–20 MeV, *EPJ Web Conf.* **154**, 01028 (2017).
- [25] N. Soppera, E. Dupont, and M. Fleming, *JANIS Book of alpha-induced cross-sections: Comparison of evaluated and experimental data from JENDL/AN-2005, TENDL-2019 and EXFOR*, Tech. Rep. (2020) OECD NEA Data Bank.
- [26] A. Oberstedt, T. Belgya, R. Billnert, R. Borcea, T. Bryś, W. Geerts, A. Göök, F.-J. Hamsch, Z. Kis, T. Martinez, S. Oberstedt, L. Szentmiklosi, K. Takács, and M. Vidali, Improved values for the characteristics of prompt-fission  $\gamma$ -ray spectra from the reaction  $^{235}\text{U}(n_{\text{th}}, f)$ , *Phys. Rev. C* **87**, 051602 (2013).
- [27] B. Buyuk, Gamma attenuation behavior of some stainless and boron steels, *Acta Phys. Pol. A* **127**, 1342 (2015).
- [28] A. J. Koning, D. Rochman, and J. -Ch. Sublet, TENDL-2021 (2021), release Date: December 30, 2021. Available from [https://tendl.web.psi.ch/tendl\\_2021/tendl2021.html](https://tendl.web.psi.ch/tendl_2021/tendl2021.html).
- [29] M. J. Berger and J. H. Hubbell, *XCOM: Photon cross sections on a personal computer*, Tech. Rep. (National Bureau of Standards, Washington, DC (USA). Center for Radiation Research, 1987).
- [30] M. Gilbert, J.-C. Sublet, and S. Dudarev, Spatial heterogeneity of tungsten transmutation in a fusion device, *Nucl. Fusion* **57**, 044002 (2017).
- [31] C. J. Werner et.al, *MCNP Users Manual - Code Version 6.2*, Tech. Rep. report LA-UR-17-29981 (Los Alamos National Laboratory, 2017) further details at <http://mcnp.lanl.gov/>.
- [32] C. J. Werner et.al, *MCNP6.2 Release Notes*, Tech. Rep. report LA-UR-18-20808 (Los Alamos National Laboratory, 2018).
- [33] G. Federici, W. Biel, M. Gilbert, R. Kemp, N. Taylor, and R. Wenninger, European DEMO design strategy and consequences for materials, *Nucl. Fus.* **57**, 092002 (2017).
- [34] M. R. Gilbert, T. Eade, T. Rey, R. Vale, C. Bachmann, U. Fischer, and N. P. Taylor, Waste implications from minor impurities in european DEMO materials, *Nucl. Fus.* **59**, 076015 (2019).
- [35] J. -Ch. Sublet, J. W. Eastwood, J. G. Morgan, M. R. Gilbert, M. Fleming, and W. Arter, FISPACT-II: An advanced simulation system for activation, transmutation and material modelling, *Nucl. Data Sheets* **139**, 77 (2017).
- [36] M. J. Lloyd, A. J. London, J. Haley, M. R. Gilbert, C. S. Becquart, C. Domain, E. Martinez, M. Moody, P. A. J. Bagot, D. Nguyen-Manh, and D. E. J. Armstrong, Interaction of transmutation products with precipitates, dislocations and grain boundaries in neutron irradiated W, *Materialia*, 101370 (2022).
- [37] J. Lilley, *Nuclear Physics, Principles and Applications*,

- 1st ed. (John Wiley & Sons, US, 2001).
- [38] J. T. Mihalcz, *Radiation detection from fission*, Tech. Rep. (Oak Ridge National Laboratory, 2004) report ORNL/TM-2004/234.
- [39] P. M. Walker and J. J. Carroll, Feature article: Nuclear isomers: Recipes from the past and ingredients for the future, *Nucl. Phys. News* **17**, 11 (2007).
- [40] M. R. Gilbert, J. Marian, and J.-C. Sublet, Energy spectra of primary knock-on atoms under neutron irradiation, *J. Nucl. Mater.* **467**, 121 (2015).
- [41] M. R. Gilbert, SPECTRA-PKA, SPECTRA-PKA is available to download from github at <https://github.com/fispact/SPECTRA-PKA>.
- [42] A. J. Koning, D. Rochman, and J. -Ch. Sublet, TENDL-2017 (2017), release Date: December 30, 2017. Available from [https://tendl.web.psi.ch/tendl\\_2017/tendl2017.html](https://tendl.web.psi.ch/tendl_2017/tendl2017.html).
- [43] R. E. MacFarlane and A. C. Kahler, Methods for processing ENDF/B-VII with NJOY, *Nucl. Data Sheets* **111**, 2739 (2010).
- [44] R. Macfarlane, D. W. Muir, R. Boicourt, A. C. Kahler III, and J. L. Conlin, *The NJOY nuclear data processing system, version 2016*, Tech. Rep. (Los Alamos National Lab.(LANL), Los Alamos, NM (United States), 2017).
- [45] M. Rieth, S. L. Dudarev, S. M. G. de Vicente, J. Aktaa, T. Ahlgren, S. Antusch, D. E. J. Armstrong, M. Balden, N. Baluc, M.-F. Barthe, W. W. Basuki, M. Batabyal, C. S. Becquart, D. Blagoeva, H. Boldryeva, J. Brinkmann, M. Celino, L. Ciupinski, J. B. Correia, A. D. Backer, C. Domain, E. Gaganidze, C. García-Rosales, J. Gibson, M. R. Gilbert, S. Giusepponi, B. Gludovatz, H. Greuner, K. Heinola, T. Höschen, A. Hoffmann, N. Holstein, F. Koch, W. Krauss, H. Li, S. Lindig, J. Linke, C. Linsmeier, P. López-Ruiz, H. Maier, J. Matejicek, T. P. Mishra, M. Muhammed, A. Muñoz, M. Muzyk, K. Nordlund, D. Nguyen-Manh, J. Opschoor, N. Ordás, T. Palacios, G. Pintsuk, R. Pippan, J. Reiser, J. Riesch, S. G. Roberts, L. Romaner, M. Rosinski, M. Sanchez, W. Schulmeyer, H. Traxler, A. Ureña, J. G. van der Laan, L. Veleva, S. Wahlberg, M. Walter, T. Weber, T. Weitkamp, S. Wurster, M. A. Yar, J. H. You, and A. Zivelonghi, Recent progress in research on tungsten materials for nuclear fusion applications in Europe, *J. Nucl. Mater.* **432**, 482 (2013).
- [46] M. Rieth, M. Dürschnabel, S. Bonk, S. Antusch, G. Pintsuk, G. Aiello, J. Henry, Y. de Carlan, B.-E. Ghidersa, H. Neuberger, J. Rey, C. Zeile, N. De Wispelaere, E. Simondon, and J. Hoffmann, Fabrication routes for advanced first wall design alternatives, *Nucl. Fusion* **61**, 116067 (2021).
- [47] D. Terentyev, M. Rieth, G. Pintsuk, J. Riesch, A. von Müller, S. Antusch, K. Mergia, E. Gaganidze, H.-C. Schneider, M. Wirtz, S. Nogami, J. Coenen, J. H. You, A. Zinovev, and W. V. Renterghem, Recent progress in the assessment of irradiation effects for in-vessel fusion materials: tungsten and copper alloys, *Nucl. Fusion* **62**, 026045 (2022).
- [48] H. Motz, Neutron capture gamma-ray spectroscopy, *Annu. Rev. Nucl. Sci.* **20**, 1 (1970).
- [49] R. Beyer, M. Dietz, D. Bemmerer, A. R. Junghans, T. Kögler, R. Massarczyk, S. Müller, K. Schmidt, R. Schwengner, T. Szücs, M. P. Takács, and A. Wagner, The  $\gamma$ -ray angular distribution in fast neutron inelastic scattering from iron, *European Phys. J. A* **54**, 58 (2018).
- [50] G. Graff, A. Lajtai, and L. Nagy, *The Angular Distribution of Gamma-Rays from the Fission of  $U^{235}$* , Tech. Rep. (International Atomic Energy Agency, 1965) IAEA Symposium on Physics and Chemistry of Fission, Salzburg, 22 - 26 March.
- [51] M. L. Goldberger and K. M. Watson, *Collision Theory* (John Wiley and Sons, New York, 1964).
- [52] R. G. Newton, *Scattering Theory of Waves and Particles* (McGraw-Hill, New York, 1966).
- [53] N. P. Kalashnikov, V. S. Remizovich, and M. I. Ryazanov, *Collisions of Fast Charged Particles in Solids* (Gordon & Breach Science Publishers, New York, 1985).
- [54] O. N. Vassiliev, *Monte Carlo Methods for Radiation Transport* (Springer, Berlin, 2017).
- [55] S. Chandrasekhar, *Radiative Transfer* (Dover, 1960).
- [56] Q. Yang and P. Olsson, Full energy range primary radiation damage model, *Phys. Rev. Mater.* **5**, 073602 (2021).
- [57] M. J. Berger, Monte Carlo calculation of the penetration and diffusion of fast charged particles, in *Methods Computat. Phys.*, Vol. 1, edited by B. Alder, S. Fernbach, and M. Rotenberg (Academic Press, New York, 1963) p. 135–215.
- [58] T. E. Booth, Common misconceptions in Monte Carlo particle transport, *Appl. Radiat. Isotopes* **70**, 1042 (2012).
- [59] L. D. Landau and E. M. Lifshitz, *The Classical Theory of Fields*, 4th ed. (Pergamon Press, Oxford, England, 1975) pp. 29 – 31.
- [60] J. H. Hubbell, W. J. Veigele, E. Briggs, R. Brown, D. Cromer, and d. R. Howerton, Atomic form factors, incoherent scattering functions, and photon scattering cross sections, *J. Phys. Chem. Ref. Data* **4**, 471 (1975).
- [61] M. Moll, H. Feick, E. Fretwurst, G. Lindström, and C. Schütze, Comparison of defects produced by fast neutrons and  $^{60}\text{Co}$ -gammas in high-resistivity silicon detectors using deep-level transient spectroscopy, *Nucl. Instrum. Methods Phys. Res. B* **388**, 335 (1997).
- [62] S. Dudarev, P. Rez, and M. Whelan, Theory of electron backscattering from crystals, *Phys. Rev. B* **51**, 3397 (1995).
- [63] H. Bethe, Bremsformel für elektronen relativistischer geschwindigkeit, *Z. Physik* **76**, 293–299 (1932).
- [64] D. R. Grimes, D. R. Warren, and M. Partridge, An approximate analytical solution of the bethe equation for charged particles in the radiotherapeutic energy range, *Sci. Reports* **7**, 9781 (2017).
- [65] M. O. El-Ghossain, Calculations of stopping power, and range of electrons interaction with different material and human body parts, *Int. J. Sci. Technol. Res.* **6**, 114 (2017).
- [66] M. J. Berger, J. S. Coursey, M. A. Zucker, *et al.*, *ESTAR, PSTAR, and ASTAR: computer programs for calculating stopping-power and range tables for electrons, protons, and helium ions (version 1.21)*, Tech. Rep. (National Institute of Standards and Technology, Gaithersburg, MD., 1999).
- [67] H. Boersch, R. Wolter, and H. Schoenebeck, Elastische Energieverluste kristallgestreuter Elektronen, *Z. Phys.* **199**, 124 (1967).
- [68] T. Fujikawa, R. Suzuki, and L. Kövér, Theory of recoil effects of elastically scattered electrons and of photoelectrons, *J. Electron Spectrosc. Related Phenomena* **151**, 170 (2006).

- [69] A. Winkelmann and M. Vos, Site-specific recoil diffraction of backscattered electrons in crystals, *Phys. Rev. Lett.* **106**, 085503 (2011).
- [70] S. L. Dudarev, Density functional theory models for radiation damage, *Annu. Rev. Mater. Res.* **43**, 35 (2013).
- [71] S. L. Dudarev, L. M. Peng, and M. J. Whelan, The effect of the surface on thermal diffuse scattering intensities in reflection high-energy electron diffraction, *Proc. R. Soc. London A* **440**, 567 (1993).
- [72] G. S. Was, *Fundamentals of radiation materials science: metals and alloys* (Springer, Berlin, 2016).
- [73] M. Boschini, C. Consolandi, M. Gervasi, S. Giani, D. Grandi, V. Ivanchenko, P. Nieminem, S. Pensotti, P. Rancoita, and M. Tacconi, An expression for the Mott cross section of electrons and positrons on nuclei with  $Z$  up to 118, *Radiat. Phys. Chem.* **90**, 39 (2013).
- [74] P. Rez, Elastic scattering of electrons by atoms, *Scan. Electron Micro.* **1982**, 43 (1982).
- [75] T. Lijian, H. Qing, and L. Zhengming, Analytic fitting to the Mott cross section of electrons, *Radiat. Phys. Chem.* **45**, 235 (1995).
- [76] D. R. Mason, D. Nguyen-Manh, and C. S. Becquart, An empirical potential for simulating vacancy clusters in tungsten, *J. Phys. Cond. Matt.* **29**, 505501 (2017).
- [77] S. Plimpton, Fast parallel algorithms for short-range molecular dynamics, *J. Comput. Phys.* **117**, 1 (1995).
- [78] P. Gordon, T. Neeraj, and M. Mendeleev, Screw dislocation mobility in bcc metals: a refined potential description for  $\alpha$ -Fe, *Philos. Mag.* **91**, 3931 (2011).
- [79] D. Mason, Incorporating non-adiabatic effects in embedded atom potentials for radiation damage cascade simulations, *J. Phys. Cond. Matt.* **27**, 145401 (2015).
- [80] M. Mendeleev, S. Han, D. Srolovitz, G. Ackland, D. Sun, and M. Asta, Development of new interatomic potentials appropriate for crystalline and liquid iron, *Philos. Mag.* **83**, 3977 (2003).
- [81] L. Malerba, M.-C. Marinica, N. Anento, C. Björkas, H. Nguyen, C. Domain, F. Djurabekova, P. Olsson, K. Nordlund, A. Serra, *et al.*, Comparison of empirical interatomic potentials for iron applied to radiation damage studies, *J. Nucl. Mater.* **406**, 19 (2010).
- [82] N. W. Ashcroft and N. Mermin, Solid state physics. london: Thomson learning (1976).
- [83] P.-W. Ma and S. Dudarev, Effect of stress on vacancy formation and migration in body-centered-cubic metals, *Phys. Rev. Mater.* **3**, 063601 (2019).
- [84] Factor  $1/6$  comes from the root mean square displacement  $\langle \mathbf{r}^2(t) \rangle = 6Dt$  computed using the three-dimensional diffusion equation  $\partial\phi(\mathbf{r}, t)/\partial t = D\nabla^2\phi(\mathbf{r}, t)$ .
- [85] C. C. Fu, E. Meslin, A. Barbu, F. Willaime, and V. Oison, Effect of  $c$  on vacancy migration in  $\alpha$ -iron, in *Solid State Phenomena*, Vol. 139 (Trans Tech Publ, 2008) pp. 157–164.
- [86] Y.-L. Liu, Z.-H. Dai, and W.-T. Wang, Influence of carbon–vacancy interaction on carbon and vacancy diffusivity in tungsten, *Computat. Mater. Sci.* **83**, 1 (2014).
- [87] M. Kabir, T. T. Lau, X. Lin, S. Yip, and K. J. V. Vliet, Effects of vacancy-solute clusters on diffusivity in metastable Fe-C alloys, *Phys. Rev. B* **82**, 134112 (2010).
- [88] M.-C. Marinica, L. Ventelon, M. R. Gilbert, L. Proville, S. L. Dudarev, J. Marian, G. Bencteux, and F. Willaime, Interatomic potentials for modelling radiation defects and dislocations in tungsten, *J. Phys. Cond. Matt.* **25**, 395502 (2013).
- [89] L. D. Landau and E. M. Lifshitz, *Quantum Mechanics, Non-relativistic theory*, 3rd ed. (Elsevier Butterworth-Heinemann, Oxford, England, 1977) pp. 579 – 583.
- [90] A. R. Allnatt and A. B. Lidiard, *Atomic Transport in Solids* (Cambridge University Press, Cambridge, England, 1993).
- [91] G. H. Vineyard, Frequency factors and isotope effects in solid state rate processes, *J. Phys. Chem. Solids* **3**, 121 (1957).
- [92] R. Landauer and J. A. Swanson, Frequency factors in the thermally activated processes, *Phys. Rev.* **121**, 1668 (1961).
- [93] M. R. Gilbert, P. Schuck, B. Sadigh, and J. Marian, Free energy generalization of the Peierls potential in iron, *Phys. Rev. Lett.* **111**, 095502 (2013).
- [94] L. Keys, J. Smith, and J. Moteff, High-temperature recovery of tungsten after neutron irradiation, *Phys. Rev.* **176**, 851 (1968).